



1 **Chemical composition and source apportionment of atmospheric aerosols on** 2 **the Namibian coast**

3 **Danitza Klopper¹, Paola Formenti², Andreas Namwoonde³, Mathieu Cazaunau², Servanne**
4 **Chevaillier², Anaïs Feron², Cécile Gaimoz², Patrick Hease², Fadi Lahmidi², Cécile Mirande-Bret²,**
5 **Sylvain Triquet², Zirui Zeng² and Stuart J. Piketh¹**

6
7 ¹ North-West University, School for Geo- and Spatial Sciences, Potchefstroom, South Africa

8 ² Laboratoire Interuniversitaire des Systèmes Atmosphériques (LISA), UMR CNRS 7583, Université Paris-
9 Est-Créteil, Université de Paris, Institut Pierre Simon Laplace, Créteil, France

10 ³ SANUMARC, University of Namibia, Henties Bay, Namibia
11

12 **Corresponding author:** paola.formenti@lisa.u-pec.fr
13

14 **Abstract**

15 The chemical composition of aerosols is of particular importance to assess their interactions with radiation,
16 clouds and trace gases in the atmosphere, and consequently their effects on air quality and the regional
17 climate. In this study, we present the results of the first long-term dataset of the aerosol chemical
18 composition at an observatory on the coast of Namibia, facing the southeast Atlantic Ocean. Aerosol samples
19 in the mass fraction of particles smaller than 10 μm in aerodynamic diameter (PM_{10}) were collected during
20 26 weeks between 2016 and 2017 at the ground-based Henties Bay Aerosol Observatory (HBAO; 22°6'S,
21 14°30'E, 30 m above mean sea level). The resulting 385 filter samples were analysed by X-ray fluorescence
22 and ion-chromatography for 24 inorganic elements and 15 water-soluble ions.

23 Statistical analysis by positive matrix factorization and back-trajectory modelling identified five major
24 sources, sea salt (mass concentration: $70.8 \pm 0.2\%$), marine biogenic ($13.5 \pm 0.8\%$), mineral dust ($9.9 \pm$
25 0.1%), secondary products ($3.2 \pm 1.0\%$) and heavy metals ($2.3 \pm 2.5\%$). While the contribution of sea salt
26 aerosol was persistent, as the dominant wind direction was south-westerly and westerly from the open
27 ocean, the occurrence of mineral dust was episodic and coincided with high wind speeds from the south-
28 southeast and the north-northwest, along the coastline. Concentrations of heavy metals measured at HBAO
29 were higher than reported in the literature from measurements over the open ocean. The heavy metals (V,
30 Cr, Nd and Mn) measured at the site were attributed to mining activities and the combustion of heavy fuels
31 in commercial ship traffic across the Cape of Good Hope sea route. Fluoride concentrations up to $25 \mu\text{g m}^{-3}$



were measured, as in heavily polluted areas in China. This is surprising and a worrisome result that has profound health implications and deserves further investigation. Although no clear signature for biomass burning could be determined, the source of secondary products identified by PMF was described by a mixture of aerosols typically emitted by biomass burning, but also by other biogenic activities. Episodic contributions with moderate correlations between NO_3^- , nss-SO_4^{2-} (higher than $2 \mu\text{g m}^{-3}$) and nss-K^+ , were observed, further indicative of the potential for an episodic source of biomass burning.

Sea salt accounted for up to 57% of the measured mass concentrations of SO_4^{2-} and the non-sea salt fraction contributed mainly to the secondary product and marine biogenic sources identified by PMF. The marine biogenic contribution is attributed to efficient oxidation in the moist marine atmosphere of sulphur-containing gas-phase emitted by marine phytoplankton in the fertile waters offshore in the Benguela Upwelling System.

The data presented in this paper provide first-ever information on the temporal variability of aerosol concentrations in the Namibian marine boundary layer and the links to meteorological conditions shaping the transport patterns of aerosols from different sources. This data can be used to provide context for intensive observations in the area.

Keywords: aerosols, chemical composition, transport, Namibia, positive matrix factorisation

1. Introduction

Atmospheric aerosol particles are emitted from both natural and anthropogenic sources. Depending on their chemical and physical characteristics, airborne aerosol particles modify the Earth's radiative budget by scattering and absorbing solar and terrestrial radiation and by altering cloud lifetime and microphysical and optical properties (Seinfeld and Pandis, 2006). The variability in their source distribution and short lifetime in the atmosphere (typically less than 10 days for particles below $1 \mu\text{m}$ in diameter, and shorter for larger particles) results in an uneven horizontal and vertical spatial distribution of concentrations and physicochemical properties (Seinfeld and Pandis, 2006). As a consequence, their effects on regional atmospheric dynamics and processes are unevenly spread and constantly changing, in stark contrast to the long-lived greenhouse gases which are well-distributed around the globe (Boucher, 2013).

The Namibian coast, and more generally the southeast Atlantic region of southern Africa, is amongst the global areas of interest to study aerosols and their role on Earth's climate (De Graaf et al., 2014; Muhlbauer et al., 2014; Painemal et al., 2014a, 2014b, 2014c; Wilcox, 2010; Zuidema et al., 2009). Local meteorological conditions in this coastal desert environment are sustained by the effect of cold ocean currents in the Benguela Upwelling System (BUS), one of the strongest oceanic upwelling systems in the world, with very low sea surface temperatures all year round, reaching a minimum in the austral winter (Cole and



64 Villacastin, 2000; Nelson and Hutchings, 1983). This has a stabilising effect on the lower troposphere,
65 resulting in the formation of a semi-permanent stratocumulus (Sc) cloud deck extending between 10–30°S,
66 10°W–10°E, that tops the marine boundary layer at ~850 hPa (Muhlbauer et al., 2014; Wood, 2015) and is
67 of global significance for Earth's radiation budget (Klein and Hartmann, 1993; Johnson et al., 2004;
68 Muhlbauer et al., 2014; Wood, 2015).

69 The region is also known for its high marine phyto- and zoo-plankton specifically in the northern BUS
70 (Louw et al., 2016). The marine biogenic activity results in the release of gaseous compounds containing
71 sulphur (dimethylsulphide (DMS), SO₂, H₂S...) to the atmosphere (Andreae et al., 1994), whose oxidation,
72 particularly in this marine environment, could produce new aerosol particles contributing to the cloud
73 droplet number concentration of the Sc clouds (Charlson et al., 1987; Andreae et al., 1995). The region is
74 also known for the seasonal transport above the Sc of optically-thick and wide-spread smoke layers of
75 biomass burning aerosols emitted from forest fires in southern Africa in the austral dry season (August to
76 October; Lindesay et al., 1996; Swap et al., 2003).

77 Despite their relevance, very limited research has been conducted to assess the seasonal cycle and long-
78 term variability of the aerosol mass concentration and chemical composition in the region (Andreae et al.,
79 1995; Annegarn et al., 1983; Dansie et al., 2017; Eltayeb et al., 1993; Formenti et al., 1999, 2003b; 2018;
80 Zorn et al., 2008). To fill this gap, the long-term surface monitoring Henties Bay Aerosol Observatory
81 (HBAO) was established in 2012 on the campus of the University of Namibia's Sam Nujoma Marine and
82 Coastal Resources Research Centre (SANUMARC), along the Namibian coast (22°S; 14°E). HBAO faces the
83 open ocean in an arid environment, far from major point sources of pollution. Episodically through the year,
84 and seasonally between April to end of July, the station is affected by polluted air masses containing light-
85 absorbing aerosols, mostly from vegetation burning (Formenti et al., 2018).

86 In this paper, we present the results of the very first long-term measurements of aerosol elemental and
87 water-soluble ionic composition from the analysis of filter samples in the mass fraction of particles smaller
88 than 10 µm in aerodynamic diameter (PM₁₀ fraction) that were collected during 26 non-consecutive
89 sampling weeks in 2016 and 2017. The paper looks into the temporal variability of measured elemental
90 and water-soluble ionic concentrations and yields the first source apportionment to the PM₁₀ loading,
91 which is linked to the synoptic pathways of air mass transport.

92 The research presented in this study is relevant to the recent intensive observational efforts that took place
93 in Namibia in 2016 and 2017 (Zuidema et al., 2016). Specifically, it provides the long-term context to the
94 intensive filter sampling that was conducted in Henties Bay as part of the Aerosols, RadiatiOn and CLOuds
95 in southern Africa (AEROCLO-sA) project (Formenti et al., 2019).




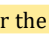

96 **2. Experimental methods**

97 The HBAO station of Henties Bay, Namibia (22.09°S, 14.26°E; 30 m above mean sea level (amsl))
98 <http://www.hbao.cnrs.fr/>, last access: 22 May 2019) is situated 100 m from the shoreline and is
99 surrounded by an arid environment with little to no vegetation, as shown in Figure 1. Henties Bay is located
100 approximately 100 km north of Walvis Bay, the largest commercial harbour of Namibia (Namport, 2018).
101 Formenti et al. (2018) showed that the location can be considered as baseline for a large part of the year
102 (August to late April). However, from May to end of July it is impacted by the synoptic transport of light-
103 absorbing aerosols mostly from vegetation burning in southern Africa and possibly but episodically by
104 anthropogenic sources, such as heavy-fuel combustion by commercial ships travelling along the coast,
105 especially along the Cape of Good Hope sea route (eg. Chance et al., 2015; Tournadre, 2014; Zhang et al.,
106 2010).

107 **2.1 Aerosol filter sampling and analysis**

108 An automated sequential air sampler (model Partisol Plus 2025i, Thermo Fisher Scientific, Waltham, MA
109 USA) was used to collect aerosol particles on 47-mm Whatman Nucleopore polycarbonate filters (1- μ m
110 pore size). Air was sampled at a flow rate of 1 m³ h⁻¹ through a certified inlet (Rupprecht and Patashnick,
111 Albany, New York, USA) located on the rooftop terrace above the instrument, and collecting aerosols
112 particles of aerodynamic diameter lower than 10 μ m (PM₁₀ fraction).

113 Individual filter samples were collected for 9 hours during the day (from 9 h to 18 h UTC) and during the
114 night (from 21 h to 6 h UTC) on an intermittent week on/week off schedule. One blank sample per time
115 series was collected. The whole dataset consisted of 385 samples.

116 Elemental concentrations of 24 elements (Na, Mg, Al, Si, P, S, Cl, K, Ca, Ti, V, Cr, Mn, Fe, Co, Ni, Cu, Zn, As, Sr,
117 Pb, Nd, Cd, Ba) were obtained at LISA by wavelength-dispersive X-ray fluorescence (WD-XRF) using a PW-
118 2404 spectrometer (Panalytical, Almelo, Netherlands), according to the protocol previously described by
119 Denjean et al. (2016). The relative analytical uncertainty on the measured atmospheric concentrations
120 (expressed in ng m⁻³) is 5%  al to the percent error on the certified mono- and bi-elemental standard
121 concentrations (Micromatter Inc., Surrey, Canada) used for calibration of the XRF apparatus.
122 Concentrations of elements from Na to Ca were corrected for  the self-attenuation effects in large particles
123 as proposed by Formenti et al. (2010). 

124 The concentrations of 16 water-soluble ions (F⁻, propionate, formate, acetate, methanesulfonic acid (MSA),
125 Cl⁻, Br⁻, NO₃⁻, PO₄³⁻, SO₄²⁻, oxalate, Na⁺, NH₄⁺, K⁺, Ca²⁺ and Mg²⁺) were obtained at LISA by ion chromatography
126 (IC) with a Metrohm IC 850 device (injection loop of 100 μ l). For anionic species, the IC was equipped with
127 MetrosepA supp 7 (250/4.0mm) column associated with a MetrosepA supp 7 guard pre-column heated at



128 45°C. For simultaneous separation of inorganic and short-chain organic anions, elution has been realised
 129 with the following elution gradient (eluent weak: $\text{Na}_2\text{CO}_3/\text{NaHCO}_3$ (0.28/0.1mM) and eluent strong:
 130 $\text{Na}_2\text{CO}_3/\text{NaHCO}_3$ (28/10mM): 100% eluent weak from 0 to 23.5 minutes; then 15% eluant strong from 23.5
 131 to 52 minutes and 100% eluent weak to finish. The elution flow rate was 0.8 ml min^{-1} . For cationic species,
 132 IC has been equipped with a Metrosep C4 (250/4.0mm) column associated to a Metrosep C4 guard column
 133 heated at 30°C. Elution has been realised with an eluant composed with 0.7 mM of dipicolinic acid and
 134 1.7mM of nitric acid. The elution flow rate was 0.9 ml min^{-1} . The uncertainty of water-soluble ionic
 135 concentrations (also expressed in ng m^{-3}) is within 5%, the maximum uncertainty obtained during
 136 calibration by standard certified mono- and multi-ionic solutions.

137 For each chemical species, the minimum quantification limit (MQL) was calculated as 10 times the square
 138 root of the standard deviation of the concentration of laboratory blank samples, corresponding to filter
 139 membranes prepared as actual samples but stored and analysed without exposure to external air. Only
 140 values above MQL are included in further analyses.

141 A quality-check assessment of the analysis was performed by comparing the concentrations of Cl, Mg, K, Ca,
 142 Na and $\text{SO}_4^{2-}/\text{S}$ measured by IC and XRF (Figure S1). The comparison revealed a good linear correlation
 143 between the two datasets, with the coefficient of determination (R^2) exceeding 0.85 for all the elements.
 144 However, some differences in the slopes of the linear correlations are observed when comparing the 2016
 145 and 2017 datasets for Cl^-/Cl , Na^+/Na , and Mg^{2+}/Mg . Slopes were 1.3 ± 0.1 (2016) and 1.0 ± 0.1 (2017), 1.3
 146 ± 0.1 (2016) and 0.9 ± 0.1 (2017), and 1.3 ± 0.1 (2016) and 1.5 ± 0.2 (2017) for Cl^-/Cl , Na^+/Na , and Mg^{2+}/Mg ,
 147 respectively. Conversely, no annual dependence was observed in the slopes of the linear correlations for
 148 Ca^{2+}/Ca (0.8 ± 0.1), K^+/K (0.8 ± 0.1) and $\text{SO}_4^{2-}/\text{S}$ (2.7 ± 0.3). These values are in general terms consistent
 149 with expectations that these elements, mostly but not exclusively composing sea salt, should be
 150 predominantly soluble in water. However, ratios higher than unity are obtained for Cl^-/Cl and Na^+/Na for
 151 2016, and Mg^{2+}/Mg for both years. Although no specific sampling nor analytical problems were found, the
 152 further comparison of their proportions to those expected for seawater (Seinfeld and Pandis, 2006)
 153 suggested to discard the XRF results and only use the values obtained by IC for those three elements. For
 154 Ca^{2+}/Ca , K^+/K and $\text{SO}_4^{2-}/\text{S}$, ratios are consistent with previous observations in marine environments
 155 impacted by mineral dust (Formenti et al., 2003a).

156 2.2 Local winds, air mass trajectories and synoptic meteorology

157 Local wind speed and direction were measured with two anemometers also located on the rooftop of HBAO,
 158 first, a Campbell Scientific 05103, replaced with a Vaisala WXT530 from September 2017 onwards.
 159 Measurements were stored as 5-minute averages. Wind data was available for all of 2016 and 55% of the
 160 aerosol sampling periods in 2017 (no wind data were available during 19 – 26 May and 7 – 14 July 2017).



161 The NOAA Hybrid Single-Particle Lagrangian Integrated Trajectory (HYSPLIT) model (Stein et al., 2015)
 162 was used to evaluate the origin and transport pathway of air masses to HBAO. Seventy-two-hour back-
 163 trajectories were run every hour for each 9-hour long filter sampling period starting at a height of 250 m
 164 above ground level (agl), which effectively models transport into the marine boundary layer (MBL, with a
 165 minimum height of ~500 m over the BUS; Preston-Whyte et al., 1977). This choice also considered the
 166 model vertical resolution (23 levels throughout the atmospheric column). The first model vertical level is
 167 at 1000 hPa (approximately 110 m amsl) and the next is at 975 hPa (approximately 300 m amsl). The Global
 168 Data Assimilation System (GDAS) reanalysis dataset with a $1^\circ \times 1^\circ$ resolution, provided by the National
 169 Centre for Environmental Prediction (NCEP), was used. This was preferred to the $0.5^\circ \times 0.5^\circ$ resolution
 170 dataset where the vertical velocity is absent and has to be calculated from the divergence, introducing
 171 uncertainties into the model. Trajectories were run through the Rstudio interface using the
 172 rich_iannone/splitR (available from <https://github.com/rich-iannone/SplitR>) and Openair (Carslaw and
 173 Ropkins, 2017) packages from the open-source libraries.

174 As a complement, publicly available daily synoptic charts provided by the South African Weather Service
 175 (SAWS, www.weathersa.co.za/home/historicalsynoptic; last accessed 20/02/2020) were analysed for the
 176 synoptic-scale induced flow.

177 3. Source identification and apportionment

178 The identification of the origin of the aerosols, complementary to the analysis of the air mass back
 179 trajectories and local wind speed and direction, was undertaken by examining the temporal correlations of
 180 the elemental and ionic concentrations to known tracers and positive matrix factorisation

181 3.1 Ratios to unique tracers

182 The identification and quantification of the aerosol types contributing to the total particle load at HBAO
 183 were done by investigating the linear correlation of measured elemental and ionic concentrations and their
 184 mass ratios to unique tracers of the atmospheric particulate matter emission sources expected in the
 185 region. These are:

- 186 • Sea salt aerosols, traced by Na^+ constituting 30.6 % of the aerosol mass in seawater (Seinfeld and
 187 Pandis, 2006);
- 188 • Marine biogenic emissions during the life cycle of marine phytoplankton in the BUS (Nelson and
 189 Hutchings, 1983) and traced by the concentrations of particulate MSA, a unique product of the
 190 oxidation of gaseous DMS (Seinfeld and Pandis, 2006);
- 191 • Wind-blown mineral dust liberated from the surface of pans and ephemeral river valleys (Annegarn
 192 et al., 1983; Eltayeb et al., 1993; Heine and Völkel, 2010; Dansie et al., 2017), but also during /road
 193 construction and mining activities (KPMG, 2014). Mineral dust is traced by elemental aluminium,



194 representing aluminosilicate minerals and contributing on average 8.13% of the global crustal rock
195 composition by mass (Seinfeld and Pandis, 2006), and by the non-sea salt (nss) fraction of Ca^{2+} to
196 represent calcium carbonate. This is justified by the specific mineralogy of Namibian soils which
197 are enriched in gypsum (CaSO_4OH) and calcite (CaCO_3), and presenting calcium content higher than
198 the world average (Annegarn et al., 1983; Eltayeb et al., 1993). The apportionment of the sea-salt
199 (ss) and non-sea salt (nss) Ca^{2+} fractions was done using the nominal mass ratio of $\text{Ca}^{2+}/\text{Na}^+$ in
200 seawater (0.021; Seinfeld and Pandis, 2006). The evaluation of the mass concentration of calcium
201 carbonate was done by multiplying the measured nss- Ca^{2+} mass concentration by the CaCO_3/Ca
202 mass ratio of 2.5;

- 203 • Elements such as Ni, V, Pb, Cu, Zn to trace heavy-oil combustion from industry and commercial
204 shipping (Becagli et al., 2017; Johansson et al., 2017; Sinha et al., 2003; Vouk and Piver, 1983) as
205 well as mining activities (Ettler et al., 2011; Křibek et al., 2018; Soto-Viruet, 2015), and;
- 206 • nss- K^+ , calculated from measured K^+ assuming the mass ratio K^+/Na^+ of 0.036 as in seawater
207 (Seinfeld and Pandis, 2006), to trace seasonal transport of biomass burning aerosols (Andreae et
208 al., 1998; Andreae and Merlet, 2001).

209 3.2 Positive matrix factorization

210 Positive matrix factorization (PMF) is a multivariate statistical method widely used to identify source
211 profiles and explore source-receptor relationships using the trace element compositions of atmospheric
212 aerosols (e.g., Schembari et al., 2014). The PMF uses weighted least-squares factor analysis to deconvolute
213 the matrix of observed values (X) as $X = G \times F + E$, where G and F are the matrices representing the factor
214 scores and factor loadings, respectively, and E is the matrix of residuals equal to the difference between
215 observed and predicted values (Paatero and Tapper, 1994; Paatero et al., 2014).

216 In this paper, the multivariate PMF statistical analysis was conducted with the EPA (Environmental
217 Protection Agency) PMF version 5.0 (Norris et al., 2014). The XRF and IC datasets were combined by
218 retaining only elements/ions measured above the MQL in more than 70 samples (that is, at least in 20% of
219 the collected values). This criterion excluded Ba, Br $^-$, PO_4^- and Mn^{2+} . Occasional missing values in the
220 retained elements/ions were replaced by the species median value, as recommended in Norris et al.,
221 (2014). Uncertainties for all missing values in the dataset were replaced by a dummy value (99999) to
222 ensure that these samples do not skew the model fit (Norris et al., 2014). According to section 5.2.1, the
223 water-soluble ionic form instead of the elemental form was retained for elemental Mg, Na, Cl, K, Ca and S.
224 SO_4^{2-} , K^+ and Ca^{2+} were included as their ss- and nss- fractions. The final matrix was made up of 385
225 observations of 33 chemical species. By comparing the signal to noise ratio, the nss- K^+ was the only species
226 in the matrix marked as a “weak basis” and on the temporal correlation, the PMF analysis resolves the chemical



dataset into a user-specified number of solution sources). No completely objective criterion exists for selecting the number of sources and so the model was run considering potential solutions of three to seven sources. Each of these models were run 100 times using randomised seeds. For each of these runs, the robustness-of-fit was compared and the estimation of the error range of each solution was done by displacing chemical species in each modelled source and testing the rotational ambiguity of the solutions (Norris et al., 2014; Paatero et al., 2014). *Fpeak* rotations with strengths between -0.5 and 1.5 were tested to further optimise the source solutions. An *Fpeak* strength of 0.5 was used for the final solution. From these analyses, the solution with the smallest uncertainties and greatest stability was selected as the most physically meaningful and representative solution.

4. Results and discussion

4.1 Meteorological conditions during sampling

The characteristic synoptic circulation patterns identified over the west coast of southern Africa that are significant for this study include continental-anticyclonic circulation, the southeast Atlantic anticyclone, west coast troughs and barotropic easterly waves, transient baroclinic westerly waves and coastal low-pressure systems (Tyson and Preston-Whyte, 2014). Formenti et al. (2018), found that anticyclonic circulation, both in the form of the South Atlantic anticyclone and the continental anticyclone, is the most persistent circulation patterns over the west coast of Namibia.

Figure 2 shows weekly composite maps of calculated air mass back trajectories (their gridded frequency plot is shown in Figure S2). Southerly and south-westerly transport occurred year-round and easterly transport mainly occurred during late autumn (May), winter (June, July and August) and early spring (September, October and November). Large scale north-easterly air mass transport towards HBAO was restricted to the austral autumn and winter when continental anticyclonic flow dominated the circulation patterns in the lower and mid-troposphere. The majority of air masses arriving in the MBL are of marine origin from the southern and south-eastern Atlantic and show the transport of marine air masses toward the subcontinent, divergence at the escarpment and southerly flow, induced along the coast. Most of the air masses were transported over coastal waters offshore and along the west coast of South Africa and Namibia and just inland to the north-northeast of HBAO from the sub-continent. Continental plumes arriving at HBAO are transported easterly between 15° and 22°S and from as far as 36°E.

Emissions along these preferred pathways may be of great significance in shaping the regional aerosol background. Some of the known transport regimes are associated with mid-tropospheric easterly winds, responsible for transport off the subcontinent (Swap et al., 1996; Tyson et al., 1996). To the north of HBAO, Adebisi and Zuidema (2016) observed continental plumes transported off the coast, especially under anticyclonic circulation over the subcontinent and the southeast Atlantic Ocean. Tlhalerwa et al. (2012)



found berg winds, an easterly perturbation, to be the main agents of aerosol transport and deposition off the coast at Luderitz, around 500 km south of HBAO, and easterly winds in the boundary layer may transport dust from the subcontinent into the ocean.

The weekly and hourly variability of local surface winds is illustrated in Figures 2 and 3, respectively. On average the wind is characterised by low speeds during the daytime ($4.7 \pm 2.2 \text{ m s}^{-1}$ with only 0.3% calm) and at night ($3.3 \pm 2.1 \text{ m s}^{-1}$ with 0.6% calm conditions). The low wind speeds are typical for regions frequently experience anticyclonic circulation. The highest wind speeds were recorded for southerly winds which were persistent throughout the sampling period, except during January 2017 (Figure 2). The highest wind speed was recorded in the austral spring in both years and reached a maximum of 18.9 m s^{-1} in the week of 13–20 November 2017.

Another feature that is promoted by anticyclonic flow is thermally-induced land and sea breezes. Sea breezes were a common daytime occurrence at HBAO. The sea breeze is typically characterised by southerly and south-westerly winds. The wind direction is partly a function of the shape of the coastline at Henties Bay and the overlying gradient flow. The daytime land breeze was not observed as frequently as the onshore sea breeze flows. This supports the conclusion that the mechanisms for onshore flow are a combination of local and large-scale circulation. ENE and northerly winds were seen in July 2016 reaching a maximum speed of 13 m s^{-1} (mean wind speed of $4.5 \pm 2.2 \text{ m s}^{-1}$ for the week of 19–26 July 2016). These are the land breezes that are also most likely to develop on clear stable nights. The northerly flow, in particular, occurred in the early evening and mid-morning (Figure 4), with no seasonal dependence. Overall, it is important to note that the sea-breeze winds during the day are well defined in the data. At night the land breeze is much less important at Henties Bay than one might expect at a coastal site. This is almost certainly driven by the small thermal gradient that exists between the ocean and land temperatures at night. In the absence of a well-defined gradient, the land breeze does not develop on most nights.

Direct westerly winds occur less frequently at the site. The winds could be observed during the day and the night indicating that they are not exclusively established as sea breeze cells. The wind speeds for westerly flow conditions never exceeded 6 m s^{-1} .

Easterly winds were only observed during the warmer months (January to March and September to December, Figure 3), and during the night-time sampling periods (21 to 9 UTC), when their speeds remained below 4 m s^{-1} (Figure 4). This local circulation is driven by easterly wave or tropical easterly circulation that moves southward during the summer months.



4.2 Variability and apportionment of measured concentrations

A summary of the measured elemental and water-soluble mass concentrations (arithmetic mean, standard deviation and range of variability) at HBAO during 2016 and 2017 are provided in Table 1. The time series of the mass concentrations of the source tracers discussed in section 3.1 are shown in Figure 5.

4.2.1 Sea salt

As expected, the major components of sea salt aerosols (Cl^- , Na^+ , Mg^{2+} and K^+) were sampled in high concentrations (up to 76, 53, 5.6 and $2.0 \mu\text{g m}^{-3}$, respectively) throughout the sampling periods. Their time variability, illustrated in Figure 5 by the example of Na^+ , was very similar and characterised by a significant continuous background that could be represented by a 10-point moving average (that is, 90 hours). The calculated mean background concentration was $10.1 \pm 3.6 \mu\text{g m}^{-3}$. No seasonal cycle was evident due to the dominance of southerly and south-westerly winds transporting marine air masses onshore (Figure 3).

Table 2 shows the mass ratios of Cl^- , Mg^{2+} , K^+ , Ca^{2+} , F^- and SO_4^{2-} to Na^+ for 2016 and 2017 calculated as the slopes of their linear regression lines, and evaluated by the coefficient of determination (R^2). The experimental values were compared with average ratios in seawater (Seinfeld and Pandis, 2006). The average Cl^-/Na^+ mass ratio was 1.35 ± 0.11 in 2016 and 1.34 ± 0.11 in 2017, lower by 25% than the value expected in seawater of 1.8. This difference has previously been reported in fresh sea salt in acidic marine environments (e.g., Zhang et al., 2010), and is attributed to Cl^- depletion via reactions between NaCl and sulfuric- and nitric acids. A very good correlation was observed between the ratios of Mg^{2+} (0.12 ± 0.01) and K^+ (0.04 ± 0.01) to Na^+ in this data set and the value reported for sea water (Table 2) and, (Seinfeld and Pandis, 2006). Conversely, the linear correlation between Ca^{2+} and Na^+ (not shown) was less pronounced ($R^2 = 0.61$ and 0.42 in 2016 and 2017, respectively). The $\text{Ca}^{2+}/\text{Na}^+$ mass ratio was systematically higher than in seawater (0.04) indicating the contribution of crustal calcium typical of the Namibian soils (see section 4.2.2). Using the average seawater ratio, the mean sea-salt (ss) Ca^{2+} concentration was estimated as $470 \pm 360 \text{ ng m}^{-3}$ and $360 \pm 210 \text{ ng m}^{-3}$ for 2016 and 2017, respectively. The mean non-sea-salt (nss) Ca^{2+} concentration was 420 ± 520 and $270 \pm 400 \text{ ng m}^{-3}$, respectively for the two years, representing 47% and 42% of the mean measured Ca^{2+} concentrations. Similarly, for both 2016 and 2017, the ss and nss components of K^+ were estimated as $367 \pm 246 \text{ ng m}^{-3}$ and $44 \pm 54 \text{ ng m}^{-3}$ respectively, accounting for 89 % and 11% of the K^+ mass. Finally, the $\text{SO}_4^{2-}/\text{Na}^+$ mass ratio for HBAO (0.36 ± 0.14) was higher than the average mass ratio for seawater (0.25). The origin and significance of this excess are explored in section 4.2.6.

4.2.2 Mineral dust

The time series of Al and nss- Ca^{2+} (Figure 5) were investigated to identify the transport of airborne mineral dust at Henties Bay. Mineral dust episodes were identified when the concentrations of those tracers



exceeded background values (modelled as the 10-point moving average) for a minimum of 3 consecutively sampled filters. Similar time variability was observed for elemental Fe, Si, Ti and P (not shown). Overall, 19 episodes of mineral dust were identified (Table S1).

The mean mass concentration of elemental Al was $556 \pm 643 \text{ ng m}^{-3}$ in 2016 and $446 \pm 551 \text{ ng m}^{-3}$ in 2017, while values peak as high as $4.7 \mu\text{g m}^{-3}$ (Table 1). To the best of our knowledge, no other measurements of Al are available in Namibia for comparison. Our nss- Ca^{2+} mean ($703 \pm 644 \text{ ng m}^{-3}$ in 2016 and $428 \pm 437 \text{ ng m}^{-3}$ in 2017) is similar to the concentrations measured by Annegarn et al. (1983) (425 ng m^{-3} and maximum of 800 ng m^{-3}) in central Namibia at Gobabeb, in the Namib Desert, ($23^{\circ}45'\text{S}$, $15^{\circ}03'\text{E}$). The annual mean Fe concentration measured at HBAO ($372 \pm 480 \text{ ng m}^{-3}$ in 2016 and $338 \pm 433 \text{ ng m}^{-3}$ in 2017) compares well with the average of 246 ng m^{-3} provided by Annegarn et al. (1983).

Table 3 shows the mass ratios for major components of mineral dust as well as some heavy metals (V and Ni). Overall, Si, Fe, and Ti showed very good correlations to Al as expected for mineral dust ($R^2 > 0.9$). The average mass ratio of Si/Al was 3.7 ± 1.0 in 2016 and 3.3 ± 0.9 in 2017, lower than the average values of 4 to 4.6 expected in global soils and crustal rock (Seinfeld and Pandis, 2006). This is attributed to the size-fractionation during aeolian erosion of soils producing airborne dust. As a matter of fact, our average values are consistent with those obtained for particles less than $10 \mu\text{m}$ in diameter by Eltayeb et al. (1993) at Gobabeb. Our averages, generally higher than in mineral dust from north Africa (Formenti et al., 2014), compare well with the value (3.4) reported by Caponi et al. (2017) for mineral dust aerosols generated in a laboratory experiment from a soil collected to the northeast of HBAO. The average Fe/Al ratio was 0.7 ± 0.2 in 2016 and 0.8 ± 0.04 in 2017, lower than the ratio of 1 reported by Eltayeb et al. (1993). The same is observed for the Ti/Al ratio, which was 0.07 ± 0.02 in 2016 and 0.06 ± 0.03 in 2017 at HBAO and approximately 0.15 in Eltayeb et al. (1993).

The average nss- Ca^{2+} /Al ratio was 1.6 ± 0.7 in 2016 and 1.4 ± 0.7 in 2017. However, for the strongest dust episodes (Al values higher than $1 \mu\text{g m}^{-3}$) the ratio tended to 1 (Figure 6). This is in agreement with the specific mineralogy of Namibian soils that are rich in limestone and gypsum (Annegarn et al., 1983; Eltayeb et al., 1993). The mean Fe/nss- Ca^{2+} ratio was 0.5 ± 0.2 in 2016 and 0.7 ± 0.2 in 2017, higher than the value of 0.11 ± 0.10 reported by Caponi et al. (2017), pointing to the diversity in soil mineralogy, even at relatively small spatial scales.

Figure 6 also shows the nss- K^{+} /Al ratios as a function of Al. As for nss- Ca^{2+} , values were spread but ranged between 0.1 and 0.5 when Al concentrations exceeded $1 \mu\text{g m}^{-3}$. These values are in agreement with those for mineral dust sources in North Africa (Formenti et al., 2014).



354 The average phosphorus concentrations measured at HBAO were $11 \pm 9 \text{ ng m}^{-3}$ in 2016 and $14 \pm 4 \text{ ng m}^{-3}$
 355 in 2017. Phosphorous was very well correlated with Al in 2016 ($R^2 = 0.92$) and only moderately correlated
 356 in 2017 ($R^2 = 0.66$). The P/Al ratio averaged 0.03 ± 0.02 in 2016 and 0.05 ± 0.02 in 2017. As was observed
 357 for the $\text{nss-Ca}^{2+}/\text{Al}$, the P/Al ratio tended to an asymptotic value of 0.02 when Al exceeded $1 \mu\text{g m}^{-3}$ (not
 358 shown). This is significantly higher than reported by Formenti et al. (2003a) for the outflow of Saharan dust
 359 to the North Atlantic Ocean (0.0070 ± 0.0004).

360 The mean concentrations of mineral dust elements Al, Fe, Ti and Si were higher for night-time sampling
 361 between 21 and 06 UTC, and lower in the day (9 to 18 UTC). It follows that the local measurement of easterly
 362 winds was only observed at night and in the early morning (Figure 4), consistent with these higher
 363 concentrations in mineral dust elements.

364 4.2.3 Heavy metals

365 Vanadium and nickel are naturally occurring in mineral deposits in soils (Annegarn et al., 1983; Maier et
 366 al., 2013), but they are also known tracers of heavy-fuel combustion, as reported in Becagli et al. (2013)
 367 and references therein. Their average concentrations at HBAO were $9 \pm 5 \text{ ng m}^{-3}$ (2016) and $7 \pm 6 \text{ ng m}^{-3}$
 368 (2017) for V, and $8 \pm 7 \text{ ng m}^{-3}$ (2016) and $7 \pm 4 \text{ ng m}^{-3}$ (2017) for Ni. These values are an order of magnitude
 369 larger than measured over the open ocean by Chance et al. (2015) and comparable to those measured by
 370 Isakson et al. (2001) at a Swedish harbour and by Becagli et al. (2012) in the central Mediterranean Sea
 371 downwind of a major shipping route. In our study, V and Ni were relatively well correlated. Vanadium was
 372 well correlated with Al when Al exceeded $1 \mu\text{g m}^{-3}$ (R^2 around 0.4), whereas no correlation between Ni and
 373 Al were observed (Figure 6). Additionally, the correlation of V to Si, also used in the literature as a tracer of
 374 mineral dust, was evident while moderate (R^2 around 0.4), while none was found for Ni. This differs from
 375 what was reported by Becagli et al. (2012), who found that neither V nor Ni were correlated to Si. In our
 376 dataset, both V/Si and Ni/Si ratios were enriched by a factor of 10 or more to reference values for the upper
 377 continental crust (3.1×10^{-4} and 1.5×10^{-4} for V/Si and Ni/Si, respectively; Henderson and Henderson, 2009).
 378 The highest V concentrations corresponded to south-south-easterly winds while the highest Ni
 379 concentrations were found for southerly to westerly winds.

380 These facts, and the moderate to good correlations of V and Ni with Zn, Cu and Pb, suggest that V and Ni do
 381 not necessarily have the same sources. Mining activities, likely in the Otavi mountain area (Boni et al.,
 382 2007), should account for the high concentrations of V, with additional contributions from combustion of
 383 heavy fuels, where V is present as an impurity (Isakson et al., 2001, and references therein; Vouk and Piver,
 384 1983). On the contrary, combustion of heavy fuels seems to be the primary source of Ni. Indeed, HBAO is
 385 located downwind one of the major ship tracks of southern Africa (Tournadre, 2014). The V/Ni ratio for




2016 is 1.7 ± 1.1 and 2017 is 1.3 ± 1.3 , lower than 2.8-2.9 reported for the central Mediterranean (Becagli et al., 2017) and 4-5 reported for a harbour in Melilla, Spain (Viana et al., 2009).

Zn and Pb are also found as impurities in bulk fuels for ships (Isakson et al., 2001). The mean concentration of Zn at HBAO ($11 \pm 9 \text{ ng m}^{-3}$) was about two orders of magnitude higher than over the southeast Atlantic Ocean (Chance et al., 2015) and in desert air (Annegarn et al., 1983). Likewise, the mean Pb concentration ($75 \pm 89 \text{ ng m}^{-3}$) was three orders of magnitude higher than reported by Chance et al. (2015) for soluble Pb and comparable to values measured in the western Mediterranean by Denjean et al. (2016). Average concentrations of Cu at HBAO were $8 \pm 6 \text{ ng m}^{-3}$, an order of magnitude higher than measured in windblown dust by Annegarn et al. (1983) in the central Namib but two orders of magnitude smaller than the average measured by Lee et al. (1999) in highly polluted Hong Kong (125.1 ng m^{-3}). Ettler et al. (2011) showed that copper ore mining and smelting operations in the Zambian Copperbelt are a significant source of potentially bioavailable copper, that, unlike phosphorus, has been found to inhibit plankton growth in laboratory studies (Paytan et al., 2009) and over the western Mediterranean (Jordi et al., 2012). Similar contamination of topsoil was found by Křibek et al. (2018) at operations in the Tsumeb mining district, Namibia ($19^{\circ}14'S$, $17^{\circ}43'E$).

4.2.4 Fluoride

Atmospheric fluoride is primarily from fluor spar mining in the Okorusu Mine ($20^{\circ}3'S$, $16^{\circ}44'E$), but very likely also from the surface mining occurring approximately 20 km south of HBAO to provide gravel for the construction of a major road between Swakopmund and Henties Bay which started late in 2015 (A. Namwoonde, *pers. corr.*). Fluoride may be leached into groundwater from fluoride-rich soils throughout the region (Wanke et al., 2015), which may then evaporate when exposed to the atmosphere.

One of the striking features of Table 1 is the high mean concentration of F⁻ measured at HBAO ($4.3 \pm 4.0 \text{ } \mu\text{g m}^{-3}$ in 2016 and $2.8 \pm 2.5 \text{ } \mu\text{g m}^{-3}$ in 2017), with peak values as high as $25 \text{ } \mu\text{g m}^{-3}$. Those annual mean concentrations were comparable to the mean 24-h fluoride concentrations measured between 1985 and 1990 over the South African Highveld by Scheifinger and Held (1997). The peak values at HBAO were significantly higher than maxima reported by these authors and ranging between 1.4 and $2.9 \text{ } \mu\text{g m}^{-3}$. The measured concentrations at HBAO were also comparable to those of heavily polluted areas in China (Feng et al., 2003), and significantly higher than reported for Europe, even in the polluted Venice lagoon (Prodi et al., 2009) or in areas nearby ceramic and glass factories (Calatrini et al., 1998). The mean F⁻/Na⁺ mass ratio measured at HBAO was 0.39 ± 0.29 in 2016 and 0.32 ± 0.29 in 2017, enriched by several orders of magnitude to average seawater composition (mass ratio 1.2×10^{-4} ;  e 2). The very good correlation of F⁻ with nss-Ca²⁺ (R^2 equal to 0.76 in 2016 and to 0.84 in 2017) yielded a mean mass ratio of 6.4 and 5.8, respectively, much higher than reported in groundwater, aerosols or precipitation in polluted



environments (Feng et al., 2003; Prodi et al., 2009). The highest F^- concentrations were associated with south to the easterly winds, that is, from the subcontinent.

4.2.5 Arsenic

Inorganic arsenic in geologic formations may be released by mining operations or evaporated from soil and groundwater (Gomez-Camirero et al., 2001). No correlation between As to Al nor $nss-Ca^{2+}$ was found. Arsenic is also released by marine algae and plankton (Sanders and Windom, 1980; Shibata et al., 1996). Again, no discernible correlation between As and MSA was found. Other sources of arsenic are biomass burning, fossil fuel combustion and non-ferrous metal smelting operations (Ahoulé et al., 2015; Gomez-Camirero et al., 2001). The arsenic concentrations at HBAO have a mean and standard deviation for 2016 of $22 \pm 16 \text{ ng m}^{-3}$ and $239 \pm 344 \text{ ng m}^{-3}$ in 2017. The mean for 2017 is skewed due to two sampling weeks with very high concentrations in the order of those measured in rural and urban-industrial areas affected by mining and smelting emission sources (Hedberg et al., 2005; Šerbula et al., 2010). For these two weeks, the MSA concentrations were slightly higher than the mean reported in Table 1 ($77 \pm 33 \text{ ng m}^{-3}$) as were the Sr concentrations ($146 \pm 53 \text{ ng m}^{-3}$). This may indicate contributions during these two weeks from marine biogenics and/or from the Tsumeb smelter in the northeast of HBAO (KPMG, 2014).

4.2.6 Sulphate and secondary aerosols

The annual mean sulphate concentration measured at HBAO was $4.1 \pm 2.6 \text{ } \mu\text{g m}^{-3}$ in 2016 and $3.4 \pm 1.4 \text{ } \mu\text{g m}^{-3}$ in 2017 (Table 4), higher than previously measured over the southern Atlantic and Pacific oceans (Zhang et al., 2010) and comparable to springtime measurements in the Venice Lagoon (Prodi et al., 2009). As shown in Formenti et al. (2019), the highest concentrations were measured in spring and autumn, while minima occurred between May and August. SO_4^{2-} and Na^+ showed good correlation ($R^2 = 0.92$ in 2016 and 0.83 in 2017, Table 2) but their mass ratios were higher than in seawater (0.36 ± 0.14 and 0.42 ± 0.23 in 2016 and 2017, respectively, compared to the expected mass ratio of 0.25 ; Seinfeld and Pandis, 2006). The apportionment of the ss and nss fractions of SO_4^{2-} was done using the nominal mass ratio of SO_4^{2-}/Na^+ in seawater (0.25 ; Seinfeld and Pandis, 2006). As a result, up to 57% of the measured SO_4^{2-} mass concentration in the PM_{10} fraction was attributed to sea salt aerosols, and the nss-component was of the order of 43%. This is in agreement with previous observations in the south Atlantic Ocean (Andreae et al., 1995; Zhang et al., 2010; Zorn et al., 2008). On the contrary, at the remote Brand se Baai site along the Atlantic coast of South Africa ($31.5^\circ\text{S } 18^\circ\text{E}$), Formenti et al. (1999) reported that sea salt accounted for about 92% of the total measured elemental sulphur concentrations.

The MSA concentrations measured at the site ranged between 10 and 230 ng m^{-3} (Table 1). The mean annual concentration was $63 \pm 39 \text{ ng m}^{-3}$, three times higher than the mean value of $20 \pm 20 \text{ ng m}^{-3}$ ($6.2 \pm 4.2 \text{ ppt}$) reported by Andreae et al. (1995) over the open ocean along 19°S , and lower than in the southeast



Atlantic Ocean (Zhang et al., 2010; Table 4). As shown by Formenti et al. (2019), the MSA concentration at HBAO displayed a clear seasonal cycle, with higher values in spring to summer, as previously observed in the Southern Hemisphere ocean due to more efficient oxidation of DMS in warmer conditions (Ayers et al., 1997; Huang et al., 2017). This also explains the highest mean concentrations of marine biogenic products (MSA, As and nss-SO_4^{2-}) measured in the morning and the lowest at night. Springtime averages for MSA were in the range of that measured by Huang et al. (2018) during a springtime cruise over the South Atlantic and by Prodi et al. (2009) in the Venice Lagoon (Table 4).

The MSA/nss-SO_4^{2-} ratio (Figure 7) displayed a large range of values (0.01 to 0.12), in agreement with values in the literature at various geographical locations, especially in the southern Hemisphere (Table 4). As pointed out by Formenti et al. (2019), the MSA/nss-SO_4^{2-} values were higher in the austral summer and spring and lower in the austral winter. This strong seasonal dependence is in agreement to that identified by Ayers et al. (1986) for marine biogenic sulphur in the Southern Hemisphere and suggests that the highest concentrations of nss-SO_4^{2-} in the PM_{10} (nss-SO_4^{2-} larger than $2 \mu\text{g m}^{-3}$) are not necessarily associated to marine biogenic emissions. From measurements at the desert station of Gobabeb, in the Namib Desert, Annegarn et al. (1983) found that only the fine mode of the bimodal distribution of sulphur aerosols, that is, that bearing the lower mass concentrations, would be due to the oxidation of sulphur-containing gaseous emissions during the marine phytoplankton life cycle.

Figure 7 also illustrates the $\text{NH}_4^+/\text{nss-SO}_4^{2-}$ mass ratio as a function of nss-SO_4^{2-} mass concentrations. Both in 2016 and 2017, the $\text{NH}_4^+/\text{nss-SO}_4^{2-}$ mass ratios were less variable than for MSA/nss-SO_4^{2-} . The annual mean $\text{NH}_4^+/\text{nss-SO}_4^{2-}$ were 0.13 ± 0.10 in 2016 and 0.14 ± 0.08 in 2017. These values are consistent with the mass ratio of 0.18 corresponding to ammonium bisulphate ($(\text{NH}_4)\text{HSO}_4$). Although some losses of NH_4^+ due to conservation on-site and transport to the laboratory in France cannot be excluded, the measured ratios are consistent with previous investigations in remote marine environments reported in Table 4, including offshore southern Africa (Andreae et al., 1995; Quinn et al., 1998).

The average $\text{NO}_3^-/\text{nss-SO}_4^{2-}$ ratio at HBAO was of the order of 0.14, significantly smaller than reported by Zhang et al. (2010) over the southeast Atlantic. Finally, poor correlation between nss-SO_4^{2-} and nss-Ca^{2+} (not shown) suggests that very little of the sulphate is present as CaSO_4 , either formed by heterogeneous deposition of SO_2 on calcite mineral particles or liberated from the soils as mineral gypsum (Annegarn et al., 1983).

Finally, the mean annual concentration of oxalate at HBAO was $72 \pm 80 \text{ ng m}^{-3}$ in 2016 and $141 \pm 50 \text{ ng m}^{-3}$ in 2017. Values at HBAO are consistent with those reported by Zhang et al. (2010) over the southeast Atlantic ($200 \pm 140 \text{ ng m}^{-3}$). Oxalate aerosols in the atmosphere are due to marine biogenic activity and



anthropogenic emissions including fossil fuel combustion and biomass burning (Gillett et al., 2007, and references therein). It is also formed by in-cloud processes and oxidation of gaseous precursors followed by condensation (Baboukas et al., 2000). The moderate correlation with NO_3^- , nss-SO_4^{2-} and nss-K^+ , particularly in 2017, could suggest a common origin and possible influence of occasional biomass burning.

4.3 Source apportionment

Figure 8 presents a summary of the five source profiles resolved by the selected PMF solution. According to their characteristic tracers, the five sources are labelled **sea salt** (Na^+ , Cl^- , F^- , Mg^{2+} , ss-SO_4^{2-} , ss-K^+ and ss-Ca^{2+}), **marine biogenic** (MSA, oxalate and As), **mineral dust** (Si, Al, Fe, Ti, F^- , nss-K^+ and nss-Ca^{2+}), **secondary products** (nss-SO_4^{2-} , NH_4^+ , formate, oxalate and nss-K^+) and **heavy metals** (V, Ni, Zn, Pb, Cr, Cu, Cd, Nd, Sr and Co). For the sake of comparison, the mass concentration of sea salt and mineral dust can also be evaluated from the chemical composition as:

$$[\text{Sea salt}] = 2.57 \cdot [\text{Na}^+], \text{ as in Zhang et al. (2010)} \quad (1a)$$

$$[\text{MD}] = [\text{Mineral dust}] = [\text{Al}]/0.0813 + 2.5 \cdot [\text{nss-Ca}^{2+}], \text{ as explained in section 3.1} \quad (1b)$$

The estimated aerosol mass (EAM) needed to evaluate their percent contributions can then be calculated as:

$$[\text{EAM}] = [\text{Sea salt}] + [\text{Mineral dust}] + [\text{other}] \quad (1c)$$

Where [other] represents the major compounds (by mass) in the input dataset, as:

$$[\text{other}] = [\text{V}] + [\text{Ni}] + [\text{Zn}] + [\text{Pb}] + [\text{Cr}] + [\text{Cu}] + [\text{nss-SO}_4^{2-}] + [\text{NH}_4^+] + [\text{MSA}] + [\text{NO}_3^-] + [\text{Oxalate}] \quad (1d)$$

4.3.1 Sea salt

Due to the location of the sampling site in this windy, coastal region, sea salts were present to some extent in all the PMF resolved sources. The sea salt source profile is described by typical elements like sodium, chloride, fluoride and magnesium ions as well as the sea salt fraction of potassium, sulphate and calcium (Figure 8). These species accounted for $70.8 \pm 0.2\%$ of the total estimated mass concentration, in good agreement with the percent contribution of the sea salt mass from Equation 1a (70.4%). In general terms, the source profile obtained by PMF is in good agreement with that obtained by chemical apportionment. In particular, the Cl^-/Na^+ mass ratio is 1.4 ± 1.6 , confirming the depletion of Cl^- with respect to Na^+ . The mass ratio of 0.11 ± 0.01 for $\text{Mg}^{2+}/\text{Na}^+$ estimated in this source was in good agreement to that reported in Table 2 and for the average seawater composition. The F^-/Na^+ mass ratio reported in Table 2 is higher than 0.19 ± 0.12 for this PMF sea salt source and this ratio is still two orders of magnitude higher than the average seawater composition reported in Seinfeld and Pandis (2006).



514 A separate PMF analysis was run with Ca^{2+} , SO_4^{2-} and K^+ ions without separating the sea salt from non-sea
515 salt components. The contributions of these elements to the sea salt aerosol mass were estimated to be 55
516 $\pm 0.1\%$ of the calcium, $60.1 \pm 0.1\%$ of the sulphate and $72.9 \pm 0.1\%$ of the potassium. This compared well to
517 the PMF solution of the dataset with the species separated by ss and nss components, indicating good
518 agreement in the apportionment by nominal mass ratios and PMF of the sea salt source.

519 4.3.2 Marine biogenic

520 The marine biogenic source profile contributed $13.5 \pm 0.8\%$ to the PM_{10} mass concentration. The source
521 profile is composed of secondary products emitted by marine biogenic processes such as MSA, oxalate and
522 As (Figure 8), which however only account for $2.8\% (\pm 0.1\%)$ of the total mass. The largest fraction of the
523 mass is contributed by Cl^- and Na^+ (combined mass contribution of $67.3 \pm 0.1\%$) and ss- and nss-sulphates
524 ($12.7 \pm 0.1\%$). The MSA/nss- SO_4^{2-} mass ratio for this source is 0.05 ± 0.25 and compares well to the chemical
525 apportionment and what was measured in the region by Andreae et al. (1995).

526 The fact that we find arsenic in this source is interesting, as it was not immediately evident from the analysis
527 of correlations between the two, but it does confirm the contributions from marine biogenic sources
528 (Sanders and Windom, 1980; Shibata et al., 1996).

529 4.3.3 Mineral dust

530 The contribution of mineral dust to the PM_{10} aerosol mass estimated by the PMF analysis is $9.9\% (\pm 0.1\%)$,
531 lower than the average of 17% calculated with Equation 1b. The difference in the estimated aerosol mass
532 is then likely explained by the use of the average aluminium content in global soils (8.13%) in the
533 calculation of estimated aerosol mass, indicating a significant difference in aluminium content of Namibian
534 soil as compared to the global average.



535 The mineral dust source profile was composed by Si, Al, Fe, Ti, F⁻, nss- K^+ and nss- Ca^{2+} (Figure 8), accounting
536 for almost all of its evaluated mass concentration ($94.9 \pm 0.1\%$). The mass contributions of P, Mn and V to
537 the source profile was small ($0.3 \pm 0.1\%$). Nevertheless, mineral dust accounts for up to 40 to 55% of their
538 variance in mass. The vanadium in this source was highly enriched to the nickel in the V/Ni mass ratio of
539 32.74 ± 0.01 , not consistent with shipping emissions reported for the Mediterranean (Becagli et al., 2017;
540 Viana et al., 2009).

541 The nss- K^+ /Al mass ratio was estimated as 0.07 ± 0.10 , lower than that obtained by chemical
542 apportionment (0.13 ± 0.12) and those reported in the literature (0.25 – 0.45, Eltayeb et al., 1993). The PMF
543 allocated $71.4 \pm 0.1\%$ of the nss- K^+ to this source and the remaining $28.4 \pm 0.1\%$ to the marine biogenic
544 and secondary products sources.



545 The $\text{nss-SO}_4^{2-}/\text{nss-Ca}^{2+}$ mass ratio was found to be 0.25 in both the PMF resolved source and the chemical
546 apportionment and was an order of magnitude lower than the mass ratio for gypsum indicating that
547 gypsum was not a main sulphate component in the region. The PMF attributed $35.8 \pm 0.1\%$ of the total Ca^{2+}
548 mass to this source, slightly lower than that calculated by nominal mass ratios for the nss-Ca^{2+} (45%). Some
549 very high concentrations in fluoride were associated with calcium and indicate a likely source of calcium
550 fluoride minerals such as fluor spar, presently mined at Okorusu mine.



551 4.3.4 Secondary products

552 The secondary products source profile,  an estimated PM_{10} aerosol mass of $3.2 \pm 1.0\%$, was  identified
553 by secondary nss-SO_4^{2-} , NH_4^+ and formate (Figure 8). These species account for $61.6 \pm 0.3\%$ of the source
554 mass. MSA, nitrate, oxalate and nss-K^+ contribute between 15 and 30% of their masses to this source and
555 together account for an additional $17.2 \pm 0.1\%$ of the source mass.

556 The $\text{NH}_4^+/\text{nss-SO}_4^{2-}$ mass ratio for this source was 0.23 ± 0.33 , consistent with ammonium bisulphate.
557 Sources of nss-SO_4^{2-} and NH_4^+ include gaseous precursors released from various biogenic and
558 anthropogenic sources, including biomass burning (Andreae et al., 1995; Behera et al., 2013; Theobald et
559 al., 2006; Zhang et al., 2010). The fact that formate, released by the oxidation of DMS and also during
560 biomass burning (Finlayson-Pitts and Pitts Jr, 2000, and references therein) was contributed to this source
561 was not surprising as it is only stable in high concentrations of ammonia (Andreae, 2000). The
562 corresponding contribution of nitrate, oxalate and nss-K^+ to this source might suggest a biomass burning
563 source (Andreae et al., 1998; Andreae and Merlet, 2001; Gillett et al., 2007), but the oxalate/ nss-SO_4^{2-} and
564 $\text{nss-K}^+/\text{nss-SO}_4^{2-}$ for this source were lower than the values reported for biomass burning emissions in
565 Formenti et al. (2003b) and Andreae et al. (1998).

566 The $\text{MSA}/\text{nss-SO}_4^{2-}$ mass ratio for this source was 0.03 ± 0.02 , inconsistent with other literature on marine
567 biogenics reported in Table 4, as opposed to the marine biogenic source identified by PMF which is in good
568 agreement with the ratio reported in Andreae et al. (1995).

569 4.3.5 Heavy metals

570 The fifth and final source profile,  $3 \pm 2.5\%$ to the total mass), was characterised by the heavy metals V,
571 Ni, Zn, Pb, Cr, Cu, Cd, Nd, Sr and Co which together contribute to $34.1 \pm 0.8\%$ of the source mass. Sea salt
572 species contributed $68.4 \pm 0.2\%$ of the mass of this source. Some of these metals were associated with 
573 mineral dust and the additional portions of these metals may be contributed by commercial shipping or
574 industrial processes, as discussed previously. The V/Ni ratio for this source was 1.00 ± 1.00 , lower than the
575 average ratios of 1.7 ± 1.1 in 2016 and 1.3 ± 1.3 in 2017 from the chemical apportionment and lower than



576 2.8 – 5 reported for different locations across the Mediterranean (Becagli et al., 2017; Schembari et al.,
577 2014; Viana et al., 2009).

578 Small amounts of nss-SO_4^{2-} were contributed to this source and the $\text{nss-SO}_4^{2-}/\text{V}$ mass ratio was 23.5 ± 1.75 ,
579 in good agreement with 16 – 24 reported by Alföldy et al., (2013) for Rotterdam harbour. Although some
580 of these heavy metals may be sourced from the commercial shipping route offshore, the mass ratios for
581 tracer elements were not in agreement with our results and so we cannot conclusively state shipping fuel
582 combustion as the source of these heavy metals.

583 **5. Conclusions and significance of results**

584 This paper presented the first long-term characterisation of the elemental and ionic composition of
585 atmospheric aerosols and the source apportionment of the PM_{10} mass fraction at the Henties Bay Aerosol
586 Observatory on the west coast of southern Africa, an under-explored region of the world to date.

587 The study was based on semi-continuous filter sampling at the HBAO site in Namibia in 2016 and 2017,
588 laboratory analysis of the collected samples by X-ray fluorescence and ion chromatography, and PMF
589 apportionment, supported by back-trajectory calculations and the analysis of local winds.

590 Trajectory analysis for the sampling period from 2016 to 2017 shows four distinct patterns of atmospheric
591 transport to HBAO. Two transport pathways are from the South Atlantic Ocean, namely directly from the
592 east and the south and south-east. A third transport pathway shows air masses reaching Henties bay from
593 the north-west. This pathway will likely include constituents that originated over the continent. The final
594 transport pathway is from central southern Africa.

595 Local wind circulation is influenced by the overlying synoptic circulation patterns as well as local sea breeze
596 mechanisms. Surface flow to HBAO is predominantly from the south and south-west. Southwesterly flow is
597 likely to be linked to sea breeze circulation as a result of thermal gradients in the daytime between the
598 desert surface and the ocean. Land and sea breezes are not common at HBAO due to a weak thermal
599 gradient at night between the ocean and desert surface.

600 In general terms, the results presented in this paper are in fair agreement with the expectations for remote
601 marine regions of the world, and previous observations in the area (Andreae et al., 1995; Zhang et al., 2010).
602 The PM_{10} aerosol load is dominated by natural species such as sea salt, mineral dust and marine biogenic
603 emissions, accounting for more than 90% of the mass. As a consequence of the proximity to the seashore of
604 the HBAO sampling station, the majority of the PM_{10} mass concentration (70%) is due to sea spray, which
605 is persistent at the diurnal and seasonal time scales.



606 For the first time, the frequency, intensity, and elemental composition of Namibian mineral dust aerosols
607 were investigated. Nineteen episodes of increased Al and nss-Ca^{2+} concentrations and lasting from one to a
608 maximum of four days were detected during the entire sampling period. This corresponds well to the
609 frequency of emission of dust plumes from river valleys, coastal sabkhas, and paleo-lacustrine sources
610 (Etosha and Makgadikgadi pans) observed by various authors (Eckardt and Kuring, 2005; Vickery et al.,
611 2013; Dansie et al., 2017). Our data series does not show any particular time dependence of the frequency
612 nor duration of the detected episodes. This is in contrast with the observation by Dansie et al. (2017) that
613 windblown dust derived from the ephemeral river valleys is transported offshore during large easterly
614 wind events, and indicative of the fact that HBAO is the receptor of mineral dust emitted by various sources.

615 One of the striking findings of this paper was the level of anthropogenic contamination and the
616 concentrations of various pollutants, including heavy metals and fluoride. Formenti et al. (2018) already
617 demonstrated a seasonal increase in the light-absorbing carbon particulate between May and late July,
618 indicative of the surface transport of biomass burning aerosols, and episodically throughout the year,
619 attributed to pollution by ship traffic along the Cape of Good Hope sea route. This work additionally
620 demonstrates that mining activities severely affect the air quality and contribute to concentrations as high
621 as, or even higher than in well-known polluted regions of the world, such as the Venice lagoon (Prodi et al.,
622 2009). The persistence of these high concentrations over the two years of sampling is extremely worrying
623 for the affected populations and needs to be addressed by dedicated investigations and decision-making
624 procedures. We suspect that some of that contamination, contributing to the highest heavy metal
625 concentrations in October 2016, might be due to the major road construction between Walvis Bay, past
626 Henties Bay and towards Angola, that started in the second half of 2016. Having said this, despite maximum
627 concentrations being measured at that time, there is no significant difference between the concentration
628 levels in 2016 (before road works) and 2017 (during the road works), suggesting that the pollution by
629 heavy metals is a specific feature in the region, which likely has implications on weather and climate. One
630 such effect could be the deposition of these metals in the ocean. While the deposition of nutrients from the
631 outflow of mineral dust could be important in fertilising waters near the coast (Dansie et al., 2017) and in
632 the Southern Ocean (Okin et al., 2011), the deposition of the trace metals (Cr, Cu, Ni, Mn, or Zn) in aerosols,
633 which play a biological role in enzymes and as structural elements in proteins (Morel and Price, 2003),
634 could also affect the marine productivity of the BUS, one of the most productive marine environments in
635 the world, and should be explored. The complexity and diversity of sources that might contribute to the
636 mineral dust load at HBAO over a year, as well as the detailed chemical composition including trace metal
637 contamination, deserve certainly further dedicated investigation.



638 The long-term time series of aerosol composition at HBAO also provides new and important insights on the
639 contribution of marine emission to the regional aerosol load. Our sampling provides the first long-term
640 measurements of the mass concentrations of MSA in the south Atlantic, and the apportionment of sulphate
641 aerosols, which are important for light scattering and cloud formation. Our data show that sea salt
642 contributes, on average, to around 57% of the total sulphate mass. The non-sea salt fraction (nss-SO_4^{2-}), of
643 the order of 43%, is partly attributed to the oxidation of sulphur-containing gaseous emissions (DMS , SO_2 ,
644 H_2S) during the marine phytoplankton life cycle, likely favoured by night-time fog and overall elevated
645 relative humidity, typical along the coast. However, nss-SO_4^{2-} mass concentrations over $2 \mu\text{g m}^{-3}$ could be
646 contributed by ship plumes as well as by episodic biomass burning. Ammonium bisulfate ($(\text{NH}_4)\text{HSO}_4$) was
647 found to be the predominant sulphate forms at HBAO, where, incidentally, we observed dramatic rusting
648 and corrosion of materials through the years. The ongoing data analysis of the AEROCLO-SA field campaign
649 will provide with further insights on the size-dependent apportionment, chemical composition and
650 hygroscopicity of sulphate aerosols.

651 **Data availability.** Original and analysed data can be obtained by email request to the corresponding author. The
652 SplitR package is found in Iannone (2018). The openair package for R is found in Carslaw and Ropkins (2017). The
653 EPA (Environmental Protection Agency) PMF version 5.0 software is available from [https://www.epa.gov/air-](https://www.epa.gov/air-research/positive-matrix-factorization-model-environmental-data-analyses)
654 [research/positive-matrix-factorization-model-environmental-data-analyses](https://www.epa.gov/air-research/positive-matrix-factorization-model-environmental-data-analyses). The NOAA Air Resources Laboratory
655 (ARL) provides the HYSPLIT transport and dispersion model and/or READY website (<http://www.ready.noaa.gov>).

656 **Author contributions.** DK, PF, SJP, AN, MC, and AF performed the filter sampling and operated the wind sensor. PH,
657 SC, FL, CMB, ST, and ZZ performed the XRF and IC analysis of the collected samples. DK performed the back-trajectory
658 calculations, analysis of wind data and PMF. DK and PF performed the analysis of the chemical analysis and integration
659 of the dataset. DK and PF wrote the paper with contributions from SJP.

660 **Competing interests.** The authors declare that they have no conflict of interest.

661 **Special issue statement.** This article is part of the special issue “New observations and related modelling studies of
662 the aerosol–cloud–climate system in the Southeast Atlantic and southern Africa regions (ACP/AMT inter-journal SI)”.
663 It is not associated with a conference.

664 **Acknowledgements.** This work receives funding by the French Centre National de la Recherche Scientifique (CNRS)
665 and the South African National Research Foundation (NRF) through the “Groupement de Recherche Internationale
666 Atmospheric Research in southern Africa and the Indian Ocean” (GDRI-ARSAIO) and the Project International de
667 Coopération Scientifique (PICS) “Long-term observations of aerosol properties in Southern Africa” (contract n.
668 260888) as well as by the Partenariats Hubert Curien (PHC) PROTEA of the French Minister of Foreign Affairs and
669 International Development (contract numbers 33913SF and 38255ZE). D. Klopper acknowledges the financial



670 support of the Climatology Research Group of North-West University and the travel scholarship of the French Embassy
671 in South Africa.



References

- Adebiyi, A.A., and Zuidema, P.: The role of the southern African easterly jet in modifying the southeast Atlantic aerosol and cloud environments, *Q. J. R. Meteorol. Soc.*, 142(697), pp. 1574–1589, doi:10.1002/qj.2765, 2016.
- Ahoulé, D.G., Lalanne, F., Mendret, J., Brosillon, S. and Maïga, A.H.: Arsenic in African Waters: A Review, *Water. Air. Soil Pollut.*, 226(9), doi:10.1007/s11270-015-2558-4, 2015.
- Alföldy, B., Balzani Lööf, J., Lagler, F., Mellqvist, J., Berg, N., Beecken, J., Weststrate, H., Duyzer, J., Bencs, L., Horemans, B., Cavalli, F., Putaud, J.-P., Janssens-Maenhout, G., Pinter Csordas, A., Van Grieken, R., Borowiak, A., Hjorth, J.: Measurements of air pollution emission factors for marine transportation. *Atmos. Meas. Tech.* 6 (7), pp. 1777 – 1791, doi: 10.5194/amt-6-1777-2013, 2013.
- Andreae, T.W., Andreae, M.O. and Schebenske, G.: Biogenic sulfur emissions and aerosols over the tropical South Atlantic 1. Dimethylsulfide in seawater and in the atmospheric boundary layer, *J. Geophys. Res.*, 99, pp. 22819–22829, doi: 10.1029/94JD01837, November 20, 1994.
- Andreae, M.O., Elbert, W. and de Mora, S.J.: Biogenic sulfur emissions and aerosols over the tropical South Atlantic: Atmospheric dimethylsulfide, aerosols and cloud condensation nuclei, *J. Geophys. Res. Atmos.*, 100(June), pp. 11335–11356, doi:10.1029/94JD02828, 1995.
- Andreae, M.O., Andreae, T.W., Annegarn, H., Beer, J., Cachier, H., Canut, P., Elbert, W., Maenhaut, W., Salma, I., Wienhold, F.G., Zenker, T. and Planck, M.: Airborne studies of aerosol emissions from savanna fires in southern Africa: 2. Aerosol chemical composition, 103(D24), pp. 119–128, doi:10.1029/98JD02280, 1998.
- Andreae, M.O., Elbert, W., Gabriel, R., Johnson, D.W., Osborne, S. and Wood, R.: Soluble ion chemistry of the atmospheric aerosol and SO₂ concentrations over the eastern North Atlantic during ACE-2, *Tellus, Ser. B Chem. Phys. Meteorol.*, 52(4), pp. 1066–1087, doi:10.1034/j.1600-0889.2000.00105.x, 2000.
- Andreae, M.O. and Merlet, P.: Emission of trace gases and aerosols from biomass burning, *Global Biogeochem. Cycles*, 15(4), pp. 955–966, doi: 10.1029/2000GB001382, 2001.
- Annegarn, H.J., van Grieken, R.E., Bibby, D.M. and von Blottnitz, F.: Background Aerosol Composition in the Namib Desert, South West Africa (Namibia), *Atmospheric Environment*, 17(10), pp. 2045–2053, doi: 10.1016/0004-6981(83)90361-X, 1983.
- Ayers, G.P., Ivey, J.P. and Goodman, H.S.: Sulfate and Methanesulfonate in the Maritime Aerosol at Cape Grim, Tasmania, *J. Atmos. Chem.*, 4, pp. 173–185, doi: 10.1007/BF00053777, 1986.
- Baboukas, E.D., Kanakidou, M. and Mihalopoulos, N.: Carboxylic acids in gas and particulate phase above the Atlantic Ocean, *J. Geophys. Res.*, 105(D11), pp. 14459–14471, doi: 10.1029/1999JD900977, 2000.
- Becagli, S., Anello, F., Bommarito, C., Cassola, F., Calzolari, G., Di Iorio, T., Di Sarra, A., Gómez-Amo, J.L., Lucarelli, F., Marconi, M., Meloni, D., Monteleone, F., Nava, S., Pace, G., Severi, M., Massimiliano Sferlazzo, D., Traversi, R. and Udisti, R.: Constraining the ship contribution to the aerosol of the central Mediterranean, *Atmos. Chem. Phys.*, 17(3), pp. 2067–2084, doi: 10.5194/acp-17-2067-2017, 2017.
- Boni, M., Terracciano, R., Evans, N.J., Laukamp, C., Schneider, J. and Bechstädt, T.: Genesis of Vanadium Ores in the Otavi Mountainland, Namibia. *Economic Geology*; 102 (3), pp. 441–469, doi: 10.2113/gsecongeo.102.3.441, 2007.
- Boucher, O.: *Atmospheric Aerosols: Properties and climate impacts*, Springer: Netherlands, 2013.
- Calatrini, F., Del Carmine, P., Lucarelli, F., Mandò, P. A., Prati, P., and Zucchiatti, A.: External-beam PIGE for fluorine determination in atmospheric aerosol, *Nuclear Instruments and Methods in Physics Research Section B: Beam Interactions with Materials and Atoms*, 136-138, pp. 975-980, doi: 10.1016/S0168-583X(97)00750-7, 1998.



- 716 Caponi, L., Formenti, P., Massabó, D., Di Biagio, C., Cazaunau, M., Pangui, E., Chevaillier, S., Landrot, G.,
 717 Andreae, O.M., Kandler, K., Piketh, S., Saeed, T., Seibert, D., Williams, E., Balkanski, Y., Prati, P. and
 718 Doussin, J.F.: Spectral- and size-resolved mass absorption efficiency of mineral dust aerosols in the
 719 shortwave spectrum: A simulation chamber study, *Atmos. Chem. Phys.*, 17(11), pp. 7175–7191,
 720 doi:10.5194/acp-17-7175-2017, 2017.
- 721 Carslaw, D. and Ropkins, K.: Package ‘openair’: Tools for the Analysis of Air Pollution Data, [online]
 722 Available from: <http://www.openair-project.org/>, <https://github.com/davidcarslaw/openair>, 2017.
- 723 Chance, R., Jickells, T.D. and Baker, A.R.: Atmospheric trace metal concentrations, solubility and deposition
 724 fluxes in remote marine air over the south-east Atlantic, *Mar. Chem.*, 177, pp. 1–12,
 725 doi:10.1016/j.marchem.2015.06.028, 2015.
- 726 Charlson, R.J., Lovelock, J.E., Andreae, M.O. and Warren, S.G.: Oceanic phytoplankton, atmospheric sulphur,
 727 cloud albedo and climate, *Nature*, 326, pp. 655–661, doi: 10.1038/326655a0, 1987.
- 728 Cole J. and Villacastin C. Sea surface temperature variability in the northern Benguela upwelling system,
 729 and implications for fisheries research, *International Journal of Remote Sensing*, 21(8), pp. 1597–1617,
 730 doi: 10.1080/014311600209922, 2000.
- 731 Dansie, A.P., Wiggs, G.F.S., Thomas, D.S.G. and Washington, R.: Measurements of windblown dust
 732 characteristics and ocean fertilization potential: The ephemeral river valleys of Namibia, *Aeolian Res.*,
 733 29(July), pp. 30–41, doi:10.1016/j.aeolia.2017.08.002, 2017.
- 734 De Graaf, M., Bellouin, N., Tilstra, L. G., Haywood, J. and Stammes, P.: Aerosol direct radiative effect of smoke
 735 over clouds over the southeast Atlantic Ocean from 2006 to 2009, *Geophys. Res. Lett.*, 41(21), pp. 7723–
 736 7730, doi:10.1002/2014GL061103, 2014.
- 737 Denjean, C., Cassola, F., Mazzino, A., Triquet, S., Chevaillier, S., Grand, N., Bourrianne, T., Momboisse, G.,
 738 Sellegri, K., Schwarzenbock, A., Freney, E., Mallet, M. and Formenti, P.: Size distribution and optical
 739 properties of mineral dust aerosols transported in the western Mediterranean, *Atmos. Chem. Phys.*,
 740 16(2), pp. 1081–1104, doi:10.5194/acp-16-1081-2016, 2016.
- 741 Eckardt, F., Kuring, N.: SeaWiFS identifies dust sources in the Namib Desert. *Int. J. Remote Sens.* 26 (19), pp.
 742 4159–4167, doi: 10.1080/01431160500113112, 2005.
- 743 Eltayeb, M.A., Van Grieken, R.E., Maenhaut, W. and Annegarn, H.J.: Aerosol-Soil Fractionation for Namib
 744 Desert Samples, *Atmos. Environ.*, 27(5), pp. 669–678, doi: 10.1016/0021-8502(92)90577-I, 1993.
- 745 Ettler, V., Mihaljevič, M., Křibek, B., Majer, V. and Šebek, O.: Tracing the spatial distribution and mobility of
 746 metal/metalloid contaminants in Oxisols in the vicinity of the Nkana copper smelter, Copperbelt
 747 province, Zambia, *Geoderma*, 164(1–2), pp. 73–84, doi:10.1016/j.geoderma.2011.05.014, 2011.
- 748 Feng, Y., Ogura, N., Feng, Z.W., Zhang, F.Z., and Shimizu, H.: The Concentrations and Sources of Fluoride in
 749 Atmospheric Depositions in Beijing, China, *Water, Air, and Soil Pollution*, 145, pp. 95–107, doi:
 750 10.1023/a:1023680112474, 2003.
- 751 Formenti, P., Piketh, S.J. and Annegarn, H.J.: Detection of non-sea salt sulphate aerosol at a remote coastal
 752 site in South Africa: A PIXE study, *Nucl. Instruments Methods Phys. Res. B*, 150, pp. 332–338, 1999.
- 753 Formenti, P., Elbert, W., Maenhaut, W., Haywood, J. and Andreae, M. O.: Chemical composition of mineral
 754 dust aerosol during the Saharan Dust Experiment (SHADE) airborne campaign in the Cape Verde region,
 755 September 2000, *J. Geophys. Res.*, 108(D18), p. 8576, doi: 10.1029/2002JD002648, 2003a.
- 756 Formenti, P., Elbert, W., Maenhaut, W., Haywood, J., Osborne, S. and Andreae, M.O.: Inorganic and
 757 carbonaceous aerosols during the Southern African Regional Science Initiative (SAFARI 2000)
 758 experiment: Chemical characteristics, physical properties, and emission data for smoke from African
 759 biomass burning, 108(Safari 2000), pp. 1–16, doi: 10.1029/2002JD002408, 2003b.



- 760 Formenti, P., Schuetz, L., Balkanski, Y., Desboeufs, K., Ebert, M. and Kandler, K.: Recent progress in
 761 understanding physical and chemical properties of mineral dust, *Atmospheric Chemistry and Physics*
 762 *Discussions*, 10, pp. 31187 – 31251, doi: 10.5194/acpd-10-31187-2010, 2010.
- 763 Formenti, P., Caquineau, S., Desboeufs, K., Klaver, A., Chevaillier, S., Journet, E. and Rajot, J.L.: Mapping the
 764 physico-chemical properties of mineral dust in western Africa: mineralogical composition. *Atmospheric*
 765 *Chemistry and Physics Discussions*, European Geosciences Union, 2014, 14 (19), pp. 10663-10686, doi:
 766 10.5194/acp-14-10663-2014, 2014.
- 767 Formenti, P., Piketh, S., Namwoonde, A., Kloppe, D., Cazaunau, M., Feron, A., Gaimoz, C., Broccardo, S.,
 768 Walton, N., Desboeufs, K., Siour, G., Burger, R., Hanghome, M., Mafwila, S., Omoregie, E., Junkermann, W.
 769 and Maenhaut, W.: Three years of measurements of light-absorbing aerosols in the marine air at Henties
 770 Bay, Namibia: seasonality, origin, and transport, *Atmos. Chem. Phys. Discuss.*, (June), pp. 1–28,
 771 doi:10.5194/acp-2017-471, 2018.
- 772 Formenti, P., D'Anna, B., Flamant, C., Mallet, M., Piketh, S.J., Schepanski, K., Waquet, F., Auriol, F., Brogniez,
 773 G., Burnet, F., Chaboureaud, J., Chauvigné, A., Chazette, P., Denjean, C., Desboeufs, K., Doussin, J., Elguindi,
 774 N., Feuerstein, S., Gaetani, M., Giorio, C., Kloppe, D., Mallet, M.D., Nabat, P., Monod, A., Solmon, F.,
 775 Namwoonde, A., Chikwililwa, C., Mushi, R., Welton, E.J. and Holben, B.: The Aerosols, Radiation and
 776 Clouds in southern Africa (AEROCLO-SA) field campaign in Namibia: overview, illustrative observations
 777 and way forward. *Bulletin of the American Meteorological Society*, [online] Available at:
 778 <https://doi.org/10.1175/BAMS-D-17-0278.1>, 2019.
- 779 Gillett, R., Galbally, I., Ayers, G., Selleck, P., Powell, J., Meyer, M., Keywood, M. and Fedele, R.: Oxalic acid and
 780 oxalate in the atmosphere. [online] Available from: [http://www.scopus.com/inward/record.url?eid=2-](http://www.scopus.com/inward/record.url?eid=2-s2.0-80053171171&partnerID=40&md5=08470ecaa392611cb869e54dddf0a16)
 781 [s2.0-80053171171&partnerID=40&md5=08470ecaa392611cb869e54dddf0a16](http://www.scopus.com/inward/record.url?eid=2-s2.0-80053171171&partnerID=40&md5=08470ecaa392611cb869e54dddf0a16), 2007.
- 782 Gomez-Camirero, A., Howe, P., Hughes, M., Kenyon, E., Lewis, D., Moore, M., Ng, J., Aitio, A. and Becking, G.:
 783 Arsenic and Arsenic Compounds, Geneva. [online] Available from:
 784 <https://apps.who.int/iris/handle/10665/42366>, 2001.
- 785 Hedberg, E., Gidhagen, L. and Johansson, C.: Source contributions to PM₁₀ and arsenic concentrations in
 786 Central Chile using positive matrix factorization, *Atmos. Environ.*, 39(3), pp. 549–561, doi:
 787 10.1016/j.atmosenv.2004.11.001, 2005.
- 788 Heine, K. and Völkel, J.: Soil Clay Minerals in Namibia and Their Significance for the Terrestrial and Marine
 789 Past Global Change Research, *Afr. Study Monogr.*, 40(March), pp. 31–50, doi: 10.14989/96299, 2010.
- 790 Henderson, P. and Henderson, G.M.: *Earth science data*, Cambridge University Press, pp. 42–44, 2009.
- 791 Huang, S., Poulain, L., Van Pinxteren, D., Van Pinxteren, M., Wu, Z., Herrmann, H. and Wiedensohler, A.:
 792 Latitudinal and Seasonal Distribution of Particulate MSA over the Atlantic using a Validated
 793 Quantification Method with HR-ToF-AMS, *Environ. Sci. Technol.*, 51(1), pp. 418–426, doi:
 794 10.1021/acs.est.6b03186, 2017.
- 795 Isakson, J., Persson, T.A. and Lindgren, E.S.: Identification and assessment of ship emissions and their effects
 796 in the harbour of Göteborg, Sweden, *Atmos. Environ.*, 35(21), pp. 3659–3666, doi: 10.1016/S1352-
 797 2310(00)00528-8, 2001.
- 798 Johansson, L., Jalkanen, J. and Kukkonen, J.: Global assessment of shipping emissions in 2015 on a high
 799 spatial and temporal resolution, *Atmos. Environ.*, 167, pp. 403–415, doi:
 800 10.1016/j.atmosenv.2017.08.042, 2017.
- 801 Johnson, B.T., Shine, K.P. and Forster, P.M.: The semi-direct aerosol effect: Impact of absorbing aerosols on
 802 marine stratocumulus, pp. 1407–1422, doi: 10.1256/qj.03.61, 2004.



- Jordi, A., Basterretxea, G., Tovar-Sanchez, A., Alastuey, A. and Querol, X.: Copper aerosols inhibit phytoplankton growth in the Mediterranean Sea, *Proc. Natl. Acad. Sci.*, 109(52), pp. 21246–21249, doi: 10.1073/pnas.1207567110, 2012.
- Klein, S.A. and Hartmann, D.L.: The Seasonal Cycle of Low Stratiform Clouds, *J. Clim.*, 6, pp. 1587–1606, doi: 10.1175/1520-0442(1993)006<1587:TSCOLS>2.0.CO;2, 1993.
- KPMG: Namibia Country mining guide: Strategy series, [online] Available from: <https://assets.kpmg.com/content/dam/kpmg/pdf/2014/09/namibia-mining-guide.pdf>, 2014.
- Kříbek, B., Šípková, A., Ettler, V., Mihaljevič, M., Majer, V., Knésl, I., Mapani, B., Penížek, V., Vaněk, A. and Sracek, O.: Variability of the copper isotopic composition in soil and grass affected by mining and smelting in Tsumeb, Namibia, *Chem. Geol.*, 493, pp. 121–135, doi: 10.1016/j.chemgeo.2018.05.035, 2018.
- Lee, E., Chan, C.K. and Paatero, P.: Application of positive matrix factorization in source apportionment of particulate pollutants in Hong Kong, 33(19), pp. 3201–3212, doi: 10.1016/S1352-2310(99)00113-2, 1999.
- Lindesay, J.A., Andreae, M.O., Goldammer, J.G., Harris, G., Annegarn, H.J., Garstang, M., Scholes, R.J. and van Wilgen, B.W.: International Geosphere-Biosphere Programme/International Global Atmospheric Chemistry SAFARI-92 field experiment: Background and overview, *J. Geophys. Res.*, 101(D19), pp. 23521–23530, doi: 10.1029/96JD01512, 1996.
- Louw, D.C., Van Der Plas, A.K., Mohrholz, V., Wasmund, N., Junker, T. and Eggert, A. Seasonal and interannual phytoplankton dynamics and forcing mechanisms in the Northern Benguela upwelling system, *J. Mar. Sys.* Elsevier B.V., 157, pp. 124–134, doi: 10.1016/j.jmarsys.2016.01.009, 2016.
- Morel, F.M.M. and Price, N.M.: The Biogeochemical Cycles of Trace Metals in the Oceans, *Science*, 300(5621), pp. 944–947, doi: 10.1126/science.1083545, 2003.
- Mühlbauer, A., McCoy, I.L. and Wood, R.: Climatology of stratocumulus cloud morphologies: Microphysical properties and radiative effects, *Atmos. Chem. Phys.*, 14(13), pp. 6695–6716, doi: 10.5194/acp-14-6695-2014, 2014.
- Namport: Annual Report, [online] Available at: https://www.namport.com.na/files/documents/dee_Annual%20Report%2012%20months%20ended%2031%20March%202018.pdf; last access 19 February 2020, 2018.
- Nelson, G. and Hutchings, L.: The Benguela upwelling area. *Prog. Oceanog.*, 12(3), 333–356, doi: 10.1016/0079-6611(83)90013-7, 1983.
- Norris, G., Duvall, R., Brown, S. and Bai, S.: EPA Positive Matrix Factorization (PMF) 5.0 Fundamentals and User Guide, Washington: U.S. Environmental Protection Agency, Office of Research and Development, 2014.
- Okin, G.S., Baker, A.R., Tegen, I., Mahowald, N.M., Dentener, F.J., Duce, R.A., Galloway, J.N., Hunter, K., Kanakidou, M., Kubilay, N., Prospero, J.M., Sarin, M., Surapipith, V., Uematsu, M., and Zhu, T.: Impacts of atmospheric nutrient deposition on marine productivity: Roles of nitrogen, phosphorus, and iron, *Global Biogeochemical Cycles*, 25(2), pp. 1–10, doi: 10.1029/2010gb003858, 2011.
- Paatero, P. and Tapper, U.: Positive Matrix Factorization: A non-negative factor model with optimal utilization of error estimates of data values, *Environmetrics*, 5(2), pp. 111–126, doi: 10.1002/env.3170050203, 1994.
- Paatero, P., Eberly, S., Brown, S.G. and Norris, G.A.: Methods for estimating uncertainty in factor analytic solutions, 7, pp. 781–797, doi: 10.5194/amt-7-781-2014, 2014.
- Painemal, D., Kato, S., Minnis, P., Funk, T., Hartmann, D.L., Short, D.A., Wilcox, E.M., Klein, S.A., Hartmann, D.L., Review, M.W., Chand, D., Wood, R., Anderson, T.L., Satheesh, S.K., Charlson, R.J., Costantino, L., Bréon,



- 848 F.M., Systems, S., Systems, S., Systems, S., Darwin, E., Espy, J.P., Muhlbauer, A., McCoy, I.L., Wood, R.,
 849 Medeiros, B., Zuidema, P., De Szoek, S., Fairall, C. and Arakawa, A.: Aerosol indirect effect on warm
 850 clouds over South-East Atlantic, from co-located MODIS and CALIPSO observations, *Atmos. Chem. Phys.*,
 851 37(13), pp. 6695–6716, doi: 10.1175/1520-0469(1980)037, 2014a.
- 852 Painemal, D., Kato, S. and Minnis, P.: Boundary layer regulation in the southeast Atlantic cloud microphysics
 853 during the biomass burning season as seen by the A-train satellite constellation, *J. Geophys. Res.*,
 854 119(19), pp. 11288–11302, doi: 10.1002/2014JD022182, 2014b.
- 855 Painemal, D., Xu, K., Cheng, A., Minnis, P. and Palikonda, R.: Mean Structure and Diurnal Cycle of Southeast
 856 Atlantic Boundary Layer Clouds: Insights from Satellite Observations and Multiscale Modeling
 857 Framework Simulations, *J. Clim.*, 28(1), pp. 324–341, doi: 10.1175/JCLI-D-14-00368.1, 2014c.
- 858 Paytan, A., Mackey, K.R.M., Chen, Y., Lima, I.D., Doney, S.C., Mahowald, N., Labiosa, R. and Post, A.F.: Toxicity
 859 of atmospheric aerosols on marine phytoplankton, *PNAS*, 106(12), pp. 4601–4605, doi:
 860 10.1073/pnas.0811486106, 2009.
- 861 Preston-Whyte, R.A., Diab, R.D. and Tyson, P.D.: Towards an inversion climatology of Southern Africa: Part
 862 II, non-surface inversions in the lower atmosphere, *South African Geogr. J.*, 59(1), pp. 45–59, doi:
 863 10.1080/03736245.1977.9713494, 1977.
- 864 Prodi, F., Belosi, F., Contini, D., Santachiara, G., Di Matteo, L., Gambaro, A., Donato, A., and Cesari, D.: Aerosol
 865 fine fraction in the Venice Lagoon: Particle composition and sources, *Atmospheric Research*, 92(2), pp.
 866 141–150, doi: 10.1016/j.atmosres.2008.09.020, 2009.
- 867 Quinn, P.K., Coffman, D.J., Kapustin, V.N., Bates, T.S. and Covert, D.S.: Aerosol optical properties in the marine
 868 boundary layer during the First Aerosol Characterization Experiment (ACE 1) and the underlying
 869 chemical and physical aerosol properties, *Journal of Geophysical Research*, 103(D13), pp. 16547–16563,
 870 1998.
- 871 Sanders, J. G. and Windom, H.L.: The uptake and reduction of arsenic species by marine algae, *Estuar. Coast.*
 872 *Mar. Sci.*, 10(5), pp. 555–567, doi: 10.1016/S0302-3524(80)80075-2, 1980.
- 873 Scheifinger, H. and Held, G.: Aerosol behaviour on the South African Highveld, *Atmos. Environ.*, 31(21), pp.
 874 3497–3509, doi: 10.1016/S1352-2310(97)00217-3, 1997.
- 875 Seinfeld, J.H. and Pandis, S.N.: *Atmospheric Chemistry and Physics: From Air Pollution to Climate Change*,
 876 2nd ed., John Wiley & Sons, Hoboken, New Jersey., 2006.
- 877 Schembari, C., Bove, M.C., Cuccia, E., Cavalli, F., Hjorth, J., Massabò, D., Nava, S., Udisti, R., and Prati, P.: Source
 878 apportionment of PM₁₀ in the Western Mediterranean based on observations from a cruise ship,
 879 *Atmospheric Environment*, 98, pp. 510–518, doi: 10.1016/j.atmosenv.2014.09.015, 2014.
- 880 Šerbula, S.M., Antonijević, M.M., Milošević, N.M., Milić, S.M. and Ilić, A.A.: Concentrations of particulate
 881 matter and arsenic in Bor (Serbia), *J. Hazard. Mater.*, 181(1–3), pp. 43–51, doi:
 882 10.1016/j.jhazmat.2010.04.065, 2010.
- 883 Shibata, Y., Sekiguchi, M., Otsuki, A. and Morita, M.: Arsenic compounds in zoo- and phyto-plankton of
 884 marine origin, *Appl. Organomet. Chem.*, 10(9), pp. 713–719, doi: 10.1002/(SICI)1099-
 885 0739(199611)10:9<713::AID-AOC536>3.0.CO;2-U, 1996.
- 886 Sinha, P., Hobbs, P.V., Yokelson, R.J., Christian, T.J., Kirchstetter, T.W. and Brientjes, R.: Emissions of trace
 887 gases and particles from two ships in the southern Atlantic Ocean, *Atmos. Environ.*, 37(15), pp. 2139–
 888 2148, doi: 10.1016/S1352-2310(03)00080-3, 2003.
- 889 Soto-Viruet, Y.: The Mineral Industries of Angola and Namibia, *U.S. Geol. Surv., Minerals Y(November)*, 1–
 890 12 [online] Available from: <https://www.usgs.gov/centers/nmic/africa-and-middle-east#na>, 2015.
- 891 South African Weather Service (SAWS): Publications. [online] Available from:
 892 <http://www.weathersa.co.za/climate/publications>. Date of access: 18 January 2017.



- 893 Stein, A.F., Draxler, R.R., Rolph, G.D., Stunder, B.J.B., Cohen, M.D. and Ngan, F.: Noaa's hysplit atmospheric
 894 transport and dispersion modeling system, *Bull. Am. Meteorol. Soc.*, 96(12), pp. 2059–2077, doi:
 895 10.1175/BAMS-D-14-00110.1, 2015.
- 896 Swap, R., Garstang, M., Macko, S.A., Tyson, P.D., Maenhaut, W., Artaxo, P., Kållberg, P. and Talbot, R.: The
 897 long-range transport of southern African aerosols to the tropical South Atlantic, *J. Geophys. Res. Atmos.*,
 898 101(D19), pp. 23777–23791, doi: 10.1029/95JD01049, 1996.
- 899 Swap, R.J., Annegarn, H.J., Suttles, J.T., King, M.D., Platnick, S., Privette, J.L. and Scholes, R.J.: Africa burning:
 900 A thematic analysis of the Southern African Regional Science Initiative (SAFARI 2000), *J. Geophys. Res.*
 901 *Atmos.*, 108(D13), p. 8465, doi: 10.1029/2003JD003747, 2003.
- 902 Theobald, M.R., Crittenden, P.D., Hunt, A.P., Tang, Y.S., Dragosits, U. and Sutton, M.A.: Ammonia emissions
 903 from a Cape fur seal colony, Cape Cross, Namibia, *Geophys. Res. Lett.*, 33(3), pp. 2–5, doi:
 904 10.1029/2005GL024384, 2006.
- 905 Tlhalerwa, K., Freiman, M.T. and Piketh, S.J.: Aerosol Deposition off the Southern African West Coast by Berg
 906 Winds, 87(2):152–161, doi: 10.1080/03736245.2005.9713838, 2012.
- 907 Tournadre, J.: Anthropogenic pressure on the open ocean: The growth of ship traffic revealed by altimeter
 908 data analysis, *Geophys. Res. Lett.*, 41(22), pp. 7924–7932, doi: 10.1002/2014GL061786, 2014.
- 909 Tyson, P.D., Garstang, M., Swap, R., Kållberg, P. and Edwards, M.: An air transport climatology for subtropical
 910 Southern Africa, *Int. J. Climatol.*, 16(3), pp. 265–291, doi: 10.1002/(SICI)1097-
 911 0088(199603)16:3<265::AID-JOC8>3.0.CO;2-M, 1996.
- 912 Tyson, P.D. and Preston-Whyte, R.A.: *The Weather and Climate of Southern Africa*, 2nd ed. Oxford University
 913 Press Southern Africa, Cape Town, 2014.
- 914 Viana, M., Amato, F., Alastuey, A., Querol, X., Moreno, T., Dos Santos, S.G., Herce, M.D. and Fernández-Patier,
 915 R.: Chemical tracers of particulate emissions from commercial shipping, *Environ. Sci. Technol.*, 43(19),
 916 pp. 7472–7477, doi: 10.1021/es901558t, 2009.
- 917 Vickery, K.J., Eckardt, F.D., Bryant, R.G.: A sub-basin scale dust plume source frequency inventory for
 918 southern Africa, 2005–2008. *Geophys. Res. Lett.* 40 (19), pp. 5274–5279, doi: 10.1002/grl.50968, 2013.
- 919 Vouk, V.B. and Piver, W.T.: Metallic Elements in Fossil Fuel Combustion Products: Amounts and Form of
 920 Emissions and Evaluation of Carcinogenicity and Mutagenicity, *Environ. Health Perspect.*, 47, pp. 201–
 921 225, doi: 10.1289/ehp.8347201, 1983.
- 922 Wanke, H., Nakwafila, A., Hamutoko, J.T., Lohe, C., Neumbo, F., Petrus, I., David, A., Beukes, H., Masule, N. and
 923 Quinger, M.: Hand dug wells in Namibia: An underestimated water source or a threat to human health?,
 924 *J. Phys. Chem. Earth*, pp. 1–10, doi: 10.1016/j.pce.2015.01.004, 2015.
- 925 Wilcox, E.M.: Stratocumulus cloud thickening beneath layers of absorbing smoke aerosol, *Atmos. Chem.*
 926 *Phys.*, 10(23), pp. 11769–11777, doi: 10.5194/acp-10-11769-2010, 2010.
- 927 Wood, R.: Stratus and stratocumulus, in *Encyclopedia of Atmospheric Sciences*, 2nd ed., vol. 2, edited by G.
 928 R. North, J. Pyle, and F. Zhang, Elsevier, pp. 196– 200, 2015.
- 929 Zhang, M., Chen, J.M., Wang, T., Cheng, T.T., Lin, L., Bhatia, R.S. and Hanvey, M.: Chemical characterization of
 930 aerosols over the Atlantic Ocean and the Pacific Ocean during two cruises in 2007 and 2008, *J. Geophys.*
 931 *Res. Atmos.*, 115(22), pp. 1–15, doi: 10.1029/2010JD014246, 2010.
- 932 Zorn, S.R., Drewnick, F., Schott, M., Hoffmann, T. and Borrmann, S.: Characterization of the South Atlantic
 933 marine boundary layer aerosol using an aerodyne aerosol mass spectrometer, *Atmos. Chem. Phys.*, 8,
 934 4711–4728 [online] Available from: www.atmos-chem-phys.net/8/4711/2008, 2008.
- 935 Zuidema, P., Painemal, D., De Szoeko, S. and Fairall, C.: Stratocumulus cloud-top height estimates and their
 936 climatic implications, *J. Clim.*, 22(17), pp. 4652–4666, doi: 10.1175/2009JCLI2708.1, 2009.



937 Zuidema, P., Redemann, J., Haywood, J., Wood, R., Piketh, S., Hipondoka, M. and Formenti, P.: Smoke and
938 Clouds above the Southeast Atlantic: Upcoming Field Campaigns Probe Absorbing Aerosol's Impact
939 on Climate, Bull. Am. Meteorol. Soc., 97, pp. 1131-1135, doi: 10.1175/BAMS-D-15-00082.1, 2016.



Table captions

Table 1. Summary statistics of elemental and water-soluble ionic concentrations measured at HBAO. The second column indicates the number of samples for which values were above the minimum quantification limit (MQL). The arithmetic means with standard deviations (sd) and range of mass concentrations (minimum and maximum) are given in ng m^{-3} .

Table 2. Annual mean mass ratios of Cl^- , Mg^{2+} , K^+ , Ca^{2+} , F^- and SO_4^{2-} with respect to Na^+ for 2016 and 2017 as well as the R^2 for each linear model and mass ratios for seawater reported in the literature (Seinfeld and Pandis; 2006). Standard deviations are indicated as *sd*.

Table 3. Average mass ratios and standard deviations for 2016 and 2017 for dust episodes. Mass ratios reported in the literature are given in the last row for comparison.

Table 4. Reported concentrations for marine biogenic and secondary aerosols for different locations, and especially in the southern hemisphere. Concentrations are in $\mu\text{g m}^{-3}$ unless stated otherwise.

Figure captions

Figure 1. Geographical map of Namibia with elevation as a shaded gradient and some of the known emission sources in the region, such as major urban settlements and airports, harbours, pans and swamps, mineral-rich mining operations, labelled by the major element begin mined, and dune fields of the Kalahari stratigraphic group (Atlas of Namibia project, 2002).

Figure 2. Composite maps of 72-hour back-trajectories for every filter sampling period in 2016 (dates in blue) and 2017 (dates in orange). From these composite maps, a clear distinction can be made between marine air masses and those of continental origin and the potential for variability from these regions in terms of distance travelled and trajectory pathway. The colours are only used to differentiate one set of trajectories from another.

Figure 3. Wind roses showing the wind speed, direction and frequency of occurrence corresponding to each aerosol sampling week in 2016 (dates in blue), and 2017 (dates in orange). The arithmetic mean wind speed for each week is reported in green. For 7–14 July 2017 no surface wind data is available.

Figure 4. Hourly wind roses during the aerosol sampling at HBAO. The arithmetic means and percentage of calm conditions, when wind speeds are below detection, is reported in green. Time is in UTC. For 7–14 July 2017 no surface wind data is available.



968 **Figure 5.** Time series (datetime in UTC) of measured concentrations for Na^+ , Ca^{2+} , Al , K^+ , SO_4^{2-} , MSA and Ni
 969 (shaded area). The solid black line indicates the calculated 10-point moving average. The sea salt (ss)
 970 components for Ca^{2+} , K^+ and SO_4^{2-} is indicated by the orange shaded areas, the non-sea salt (nss) fraction is
 971 represented by the blue shaded areas. The time series is non-consecutive and is divided into the 26
 972 sampling weeks by the light grey vertical lines.

973 **Figure 6.** Scatterplots of $\text{nss-Ca}^{2+}/\text{Al}$ (top left), $\text{nss-K}^+/\text{Al}$ (top right), V (bottom left) and Ni (bottom right)
 974 ratios to Al for 2016 (blue) and 2017 (orange). Concentrations are expressed in $\mu\text{g m}^{-3}$. Note the logarithmic
 975 y-axes on the top plots.

976 **Figure 7.** Scatterplots for ratios of MSA (left) and NH_4^+ (right) to nss-SO_4^{2-} for 2016 (blue) and 2017
 977 (orange). Concentrations are expressed in $\mu\text{g m}^{-3}$. Note the logarithmic y-axis of the figure on the right.

978 **Figure 8.** Profiles of the five sources identified by the PMF analysis. Blue bars denote the mass
 979 concentrations of individual elements/ionic species (left logarithmic axis, ng m^{-3}) while the yellow points
 980 indicate the percent of species attributed to the source (right axis).

981



Table 1. Summary statistics of elemental and water-soluble ionic concentrations measured at HBAO. The second column indicates the number of samples for which values were above the minimum quantification limit (MQL). The arithmetic means with standard deviations (sd) and range of mass concentrations (minimum and maximum) are given in ng m^{-3} .

Chemical species	Number of samples	Mean \pm sd	Range
Cl	385	13216 \pm 7987	17 - 50041
S	383	1346 \pm 645	1 - 4386
Ca	366	885 \pm 768	75 - 6862
Fe	383	367 \pm 458	3 - 3687
Na	380	8435 \pm 5752	18 - 42688
Mg	380	1178 \pm 792	1 - 6416
Al	379	478 \pm 581	2 - 4739
Si	374	1687 \pm 2102	5 - 17016
P	352	10 \pm 8	1 - 72
K	379	511 \pm 359	8 - 3076
Ti	367	39 \pm 47	1 - 363
Mn	295	13 \pm 11	1 - 86
Zn	182	12 \pm 7	1 - 42
Cr	228	8 \pm 6	1 - 31
V	334	8 \pm 5	1 - 38
Ba	100	9 \pm 7	1 - 34
Co	261	8 \pm 5	1 - 32
Cu	228	13 \pm 9	1 - 48
Nd	296	15 \pm 11	1 - 61
Ni	278	8 \pm 6	1 - 33
Sr	251	77 \pm 63	2 - 346
Cd	214	735 \pm 1124	1 - 6776
As	221	191 \pm 317	1 - 1092
Pb	193	75 \pm 89	1 - 509
F ⁻	375	3356 \pm 3201	110 - 25240
Acetate	90	27 \pm 36	11 - 235
Propionate	79	46 \pm 21	12 - 162
Formate	322	23 \pm 12	5 - 73
MSA	330	63 \pm 38	11 - 232
Cl ⁻	376	13980 \pm 9834	117 - 76008
Br ⁻	17	44 \pm 15	27 - 77
NO ₃ ⁻	364	232 \pm 432	26 - 8167
PO ₄ ⁻	41	60 \pm 62	27 - 397
SO ₄ ²⁻	376	3602 \pm 1853	81 - 14331
Oxalate	379	121 \pm 53	13 - 474
Na ⁺	376	10199 \pm 6853	32 - 52987
NH ₄ ⁺	376	205 \pm 126	25 - 1747
K ⁺	373	413 \pm 265	23 - 1976
Mn ²⁺	7	41 \pm 35	22 - 117
Ca ²⁺	371	727 \pm 618	35 - 5232
Mg ²⁺	370	1168 \pm 768	29 - 5585



Table 2. Annual mean mass ratios of Cl^- , Mg^{2+} , K^+ , Ca^{2+} , F^- and SO_4^{2-} with respect to Na^+ for 2016 and 2017 as well as the R^2 for each linear model and mass ratios for seawater reported in the literature (Seinfeld and Pandis; 2006). Standard deviations are indicated as *sd*.

	2016		2017		Average seawater
	Mass ratio \pm sd	R^2	Mass ratio \pm sd	R^2	Mass ratio
Cl^-/Na^+	1.35 ± 0.11	0.99	1.34 ± 0.11	0.99	1.80
$\text{Mg}^{2+}/\text{Na}^+$	0.12 ± 0.01	0.99	0.11 ± 0.01	0.99	0.12
K^+/Na^+	0.04 ± 0.01	0.98	0.04 ± 0.01	0.93	0.04
$\text{Ca}^{2+}/\text{Na}^+$	0.07 ± 0.04	0.61	0.07 ± 0.05	0.42	0.04
$\text{SO}_4^{2-}/\text{Na}^+$	0.36 ± 0.14	0.95	0.42 ± 0.23	0.85	0.25
F^-/Na^+	0.38 ± 0.24	0.53	0.32 ± 0.35	0.33	0.000122



Table 3. Average mass ratios and standard deviations for 2016 and 2017 for dust episodes. Mass ratios reported in the literature are given in the last row for comparison.

	2016		2017		Dust episodes		Literature values
	Mean (\pm sd)	R^2	Mean (\pm sd)	R^2	Mean (\pm sd)	R^2	
Si/Al	3.75 \pm 1.04	0.96	3.51 \pm 0.74	0.96	3.60 \pm 0.65	0.94	2.87 – 6.13 ^a , 3.41 ^b , 4.63 ^c
nss-Ca ²⁺ /Al	1.27 \pm 0.67	0.89	0.5 \pm 0.37	0.83	1.42 \pm 0.87	0.60	0.35 – 6.06 ^a , 0.19 ^c
Fe/Al	0.75 \pm 0.19	0.96	0.81 \pm 0.20	0.97	0.81 \pm 0.11	0.97	0.65 – 1.06 ^b , 0.53 ^c
V/Al	0.03 \pm 0.03	0.37	0.03 \pm 0.04	0.26	0.02 \pm 0.03	0.31	0.0014 ^c
Ti/Al	0.07 \pm 0.22	0.96	0.1 \pm 0.04	0.97	0.08 \pm 0.02	0.97	0.09 – 0.15 ^a , 0.07 ^c
P/Al	0.03 \pm 0.02	0.81	0.03 \pm 0.03	0.59	0.02 \pm 0.01	0.72	0.007 ^d
Fe/nss-Ca ²⁺	0.66 \pm 0.23	0.94	2.73 \pm 25.81	0.83	8.57 \pm 77.71	0.60	0.18 – 1.86 ^a , 0.58 ^b , 2.77 ^c
nss-K ⁺ /Al	0.13 \pm 0.12	0.81	0.13 \pm 0.13	0.59	0.08 \pm 0.06	0.61	0.251 – 0.452 ^a
V/Si	0.01 \pm 0.01	0.39	0.01 \pm 0.01	0.26	0.01 \pm 0.01	0.33	0.0003 ^c
F-/Al	11.75 \pm 8.40	0.73	9.66 \pm 8.38	0.64	6.90 \pm 4.56	0.57	–
nss-SO ₄ ²⁻ / nss-Ca ²⁺	5.32 \pm 6.79	0.08	8.72 \pm 44.24	0.03	3.21 \pm 5.73	0.11	2.4 ^e

^a Eltayeb et al., (1993) from various sites around the Central Namib

^b Annegarn et al. (1983): Gobabeb, Namibia

^c Seinfeld and Pandis (2006): average chemical composition for soils globally

^d Formenti et al., (2003): Cape Verde region

^e Molar mass ratio for gypsum



Table 4. Reported concentrations for marine biogenic and secondary aerosols for different locations, and especially in the southern hemisphere. Concentrations are in $\mu\text{g m}^{-3}$ unless stated otherwise.

	SO_4^{2-} (nss- SO_4^{2-})	NH_4^+	NO_3^-	MSA	MSA/nss- SO_4^{2-}
Outflow Africa south of Cape Town, PM1^a	1.39	0.18	0.01	0.04	0.007 ^{aaa}
Southern Ocean south of Australia^b	-	-	-	0.02 - 0.2	0.24 ± 0.16
Cape Grim, Tasmania^c	11.9 ± 1.2 nmole/m ³	-	-	0.167 ± 0.027 nmole/m ³	0.063 ± 0.020
19°S offshore southern Africa^d	-	-	-	6.1 ± 4 ppt; 6.3 ± 4.4 ppt	0.05 - 0.11
Southern Atlantic^e A = autumn, S = spring	1.95 ± 1.05 ^e	7.6 ± 13.9 ^e	1.05 ± 0.72 ^e	0.21 ± 0.30 ^e S: 0.05 ± 0.1 ^j A: 0.15 ± 0.1 ^j	0.11 ^e
Southern Pacific^e	2.10 ± 1.05	0 ± 0	0.12 ± 0.15	0.58 ± 0.60	0.27
Venice Lagoon^g W = winter, S = spring	W: 3.3 ± 1.0; S: 4.4 ± 1.2	W: 2.9 ± 0.6 S: 2.6 ± 1.0	W: 9.0 ± 2.4 S: 3.5 ± 2.9	W: 0.035 ± 0.017 S: 0.054 ± 0.040	0.1
Southern Indian Ocean^h	-	-	-	-	0.1
America Samoa (14°S, 170°W)ⁱ	-	-	-	-	0.06
Coastal Antarctica^j	-	-	-	-	0.05 - 0.17
This study; 2016	4.0 ± 2.4 (1.7 ± 0.8)	0.19 ± 0.10	0.26 ± 0.71	0.07 ± 0.01	0.03 ± 0.01
This study; 2017	3.4 ± 1.4 (1.6 ± 0.7)	0.20 ± 0.10	0.22 ± 0.12	0.07 ± 0.04	0.04 ± 0.02

^a Zorn et al. (2008); PM1 fraction, ^{aaa} calculated with respect to total sulphate

^b Quinn et al. (1998)

^c Ayers et al. (1986)

^d Andreae et al. (1995)

^e Zhang et al. (2010); total suspended particulates fraction

^f Huang et al. (2016)

^g Prodi et al. (2009)

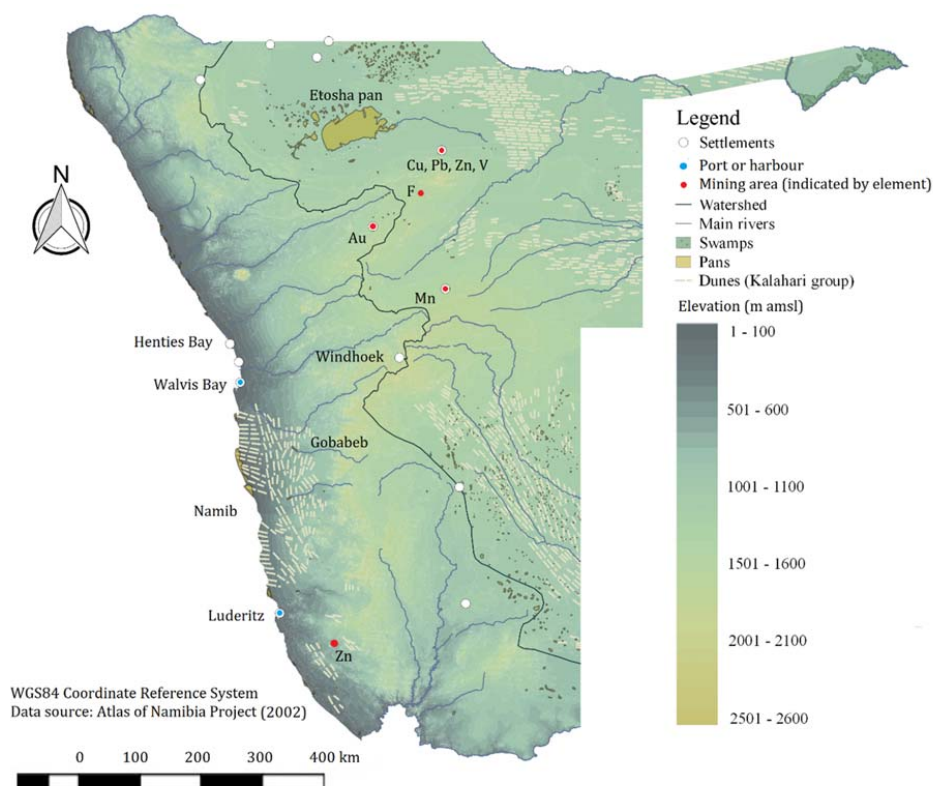
^h Sciare et al. (2000)

ⁱ Savoie et al. (1994)

^j Chen et al. (2012)

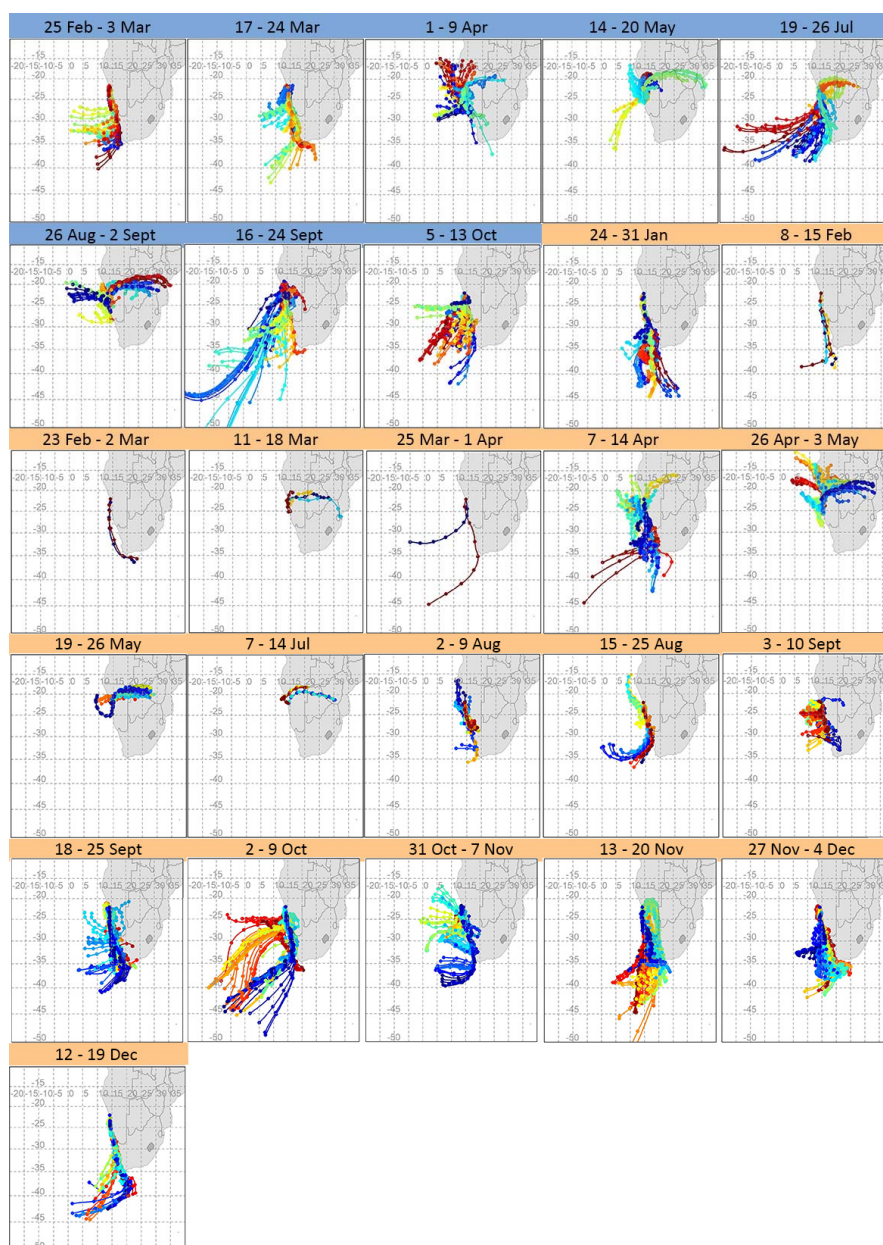


1017 **Figure 1.** Geographical map of Namibia with elevation as a shaded gradient and some of the known emission sources in
 1018 the region, such as major urban settlements and airports, harbours, pans and swamps, mineral-rich mining operations,
 1019 labelled by the major element begin mined, and dune fields of the Kalahari stratigraphic group (Atlas of Namibia project,
 1020 2002).



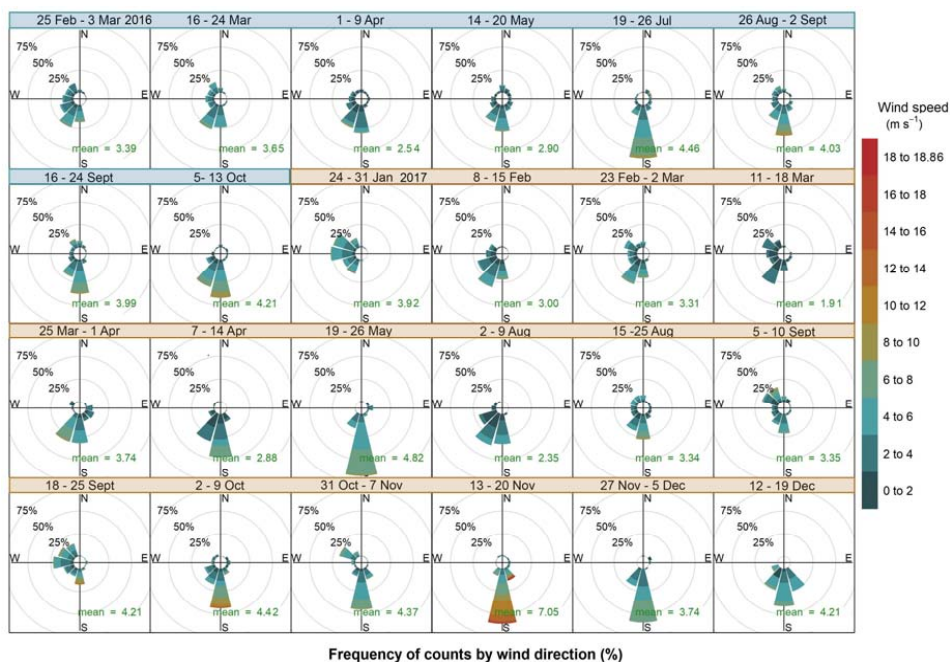


1024 **Figure 2.** Composite maps of 72-hour back-trajectories for every filter sampling period in 2016 (dates in blue) and 2017
 1025 (dates in orange). From these composite maps, a clear distinction can be made between marine air masses and those of
 1026 continental origin and the potential for variability from these regions in terms of distance travelled and trajectory
 1027 pathway. The colours are only used to differentiate one set of trajectories from another.



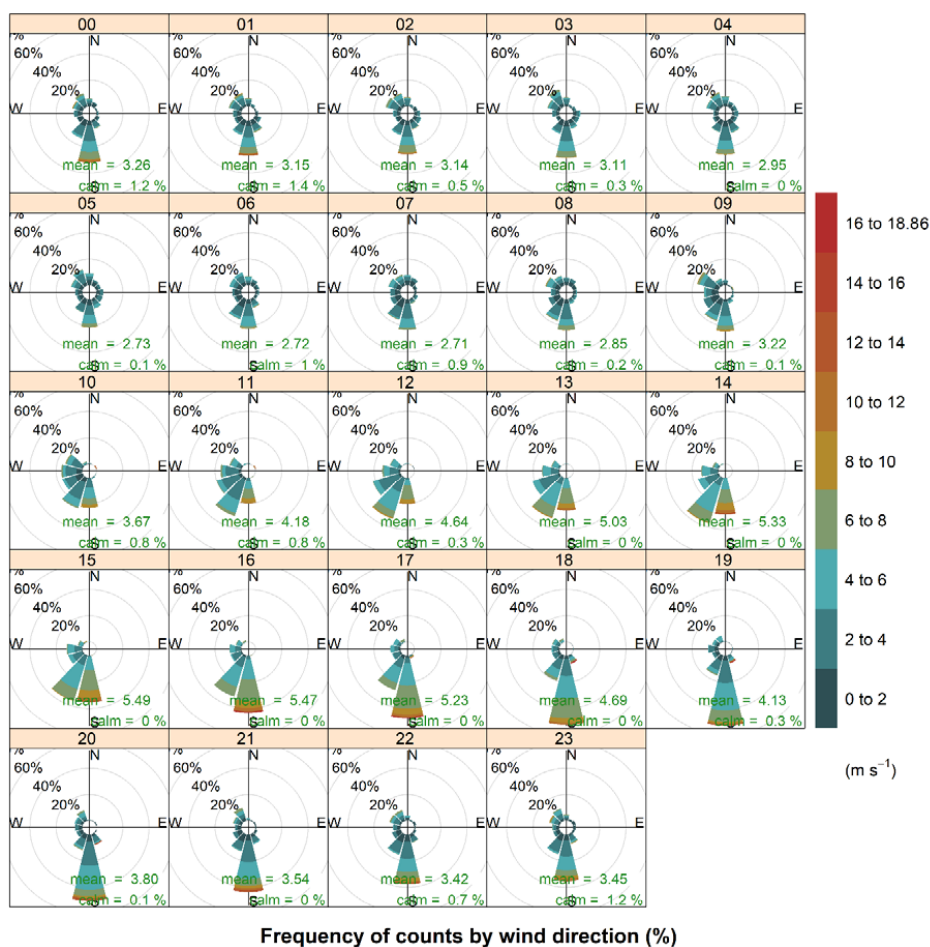


1029 **Figure 3.** Wind roses showing the wind speed, direction and frequency of occurrence corresponding to each aerosol
 1030 sampling week in 2016 (dates in blue), and 2017 (dates in orange). The arithmetic mean wind speed for each week is
 1031 reported in green. For 7–14 July 2017 no surface wind data is available.



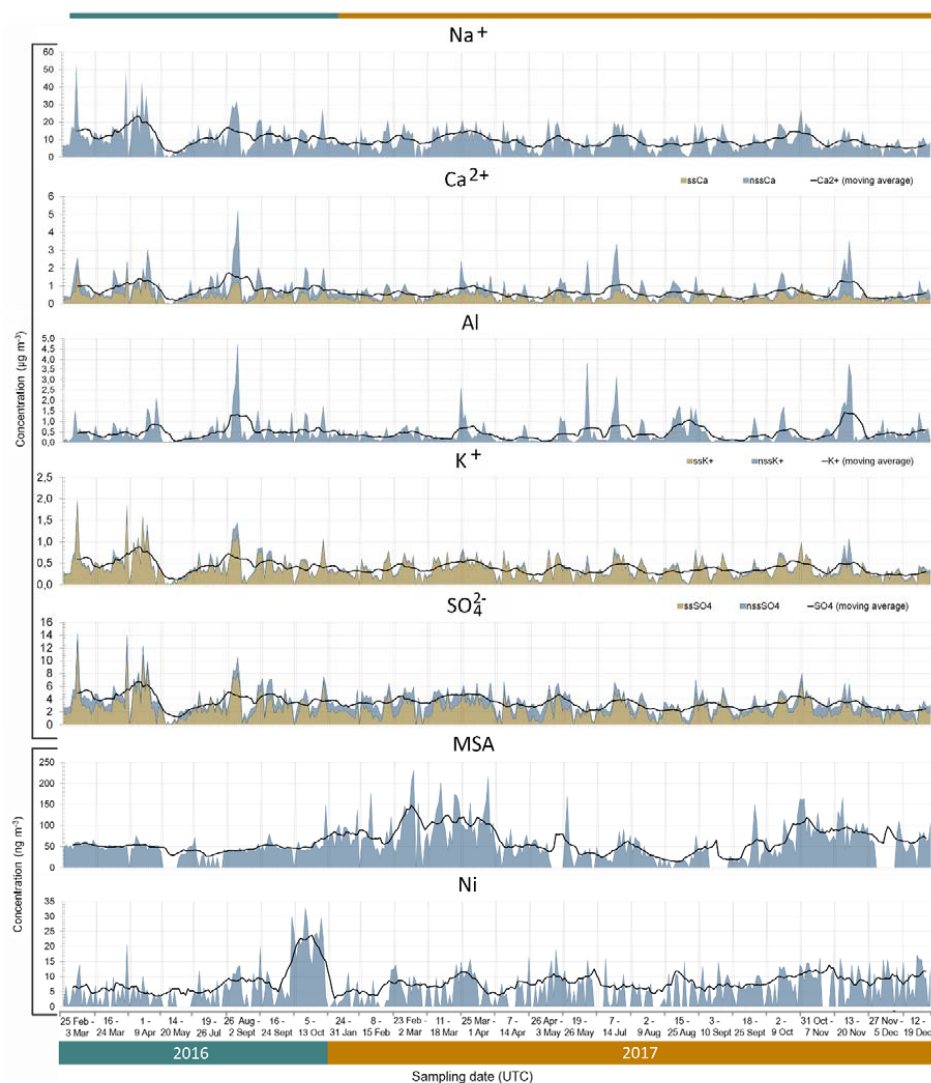


1034 **Figure 4.** Hourly wind roses during the aerosol sampling at HBAO. The arithmetic means and percentage of calm
 1035 conditions, when wind speeds are below detection, is reported in green. Time is in UTC. For 7–14 July 2017 no surface
 1036 wind data is available.





1039 **Figure 5.** Time series (datetime in UTC) of measured concentrations for Na^+ , Ca^{2+} , Al , K^+ , SO_4^{2-} , MSA and Ni (shaded area).
 1040 The solid black line indicates the calculated 10-point moving average. The sea salt (ss) components for Ca^{2+} , K^+ and SO_4^{2-}
 1041 is indicated by the orange shaded areas, the non-sea salt (nss) fraction is represented by the blue shaded areas. The time
 1042 series is non-consecutive and is divided into the 26 sampling weeks by the light grey vertical lines.

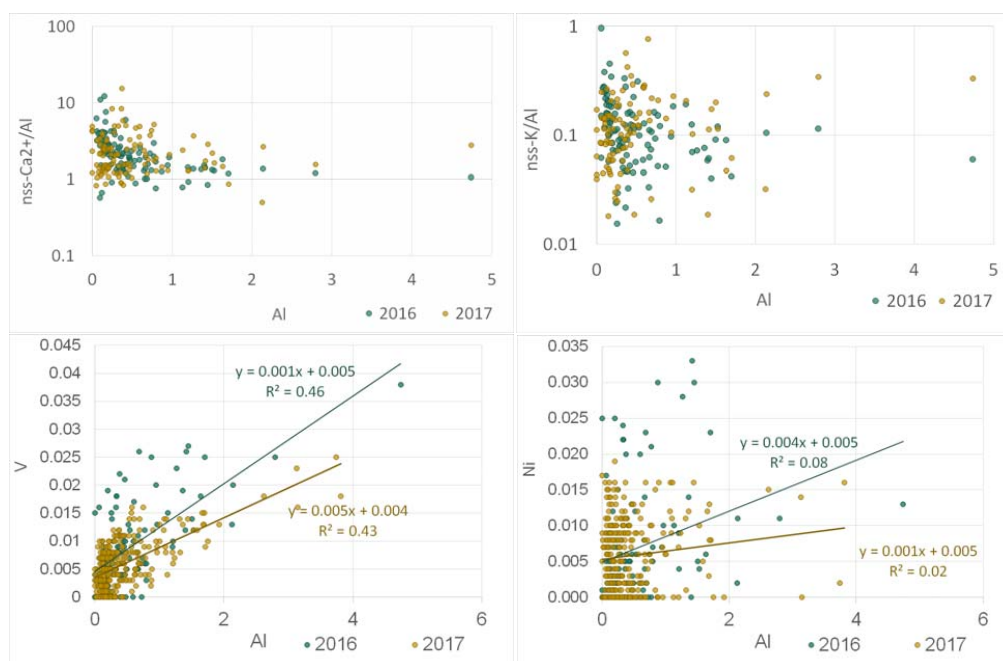


1043

1044

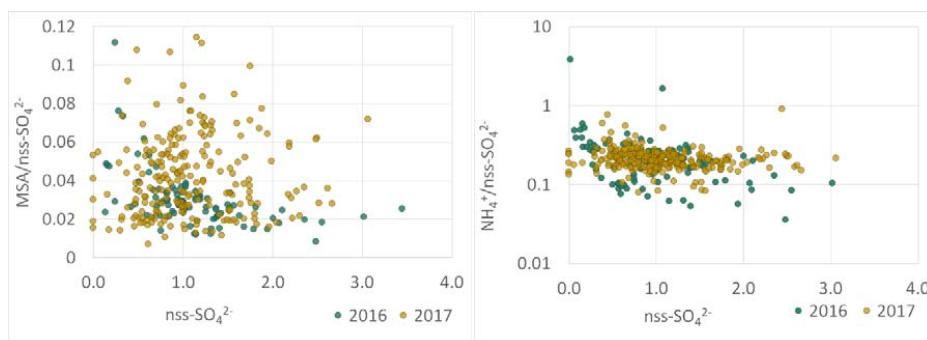


Figure 6. Scatterplots of $nss\text{-Ca}^{2+}/\text{Al}$ (top left), $nss\text{-K}^+/\text{Al}$ (top right), V (bottom left) and Ni (bottom right) ratios to Al for 2016 (blue) and 2017 (orange). Concentrations are expressed in $\mu\text{g m}^{-3}$. Note the logarithmic y-axes on the top plots.



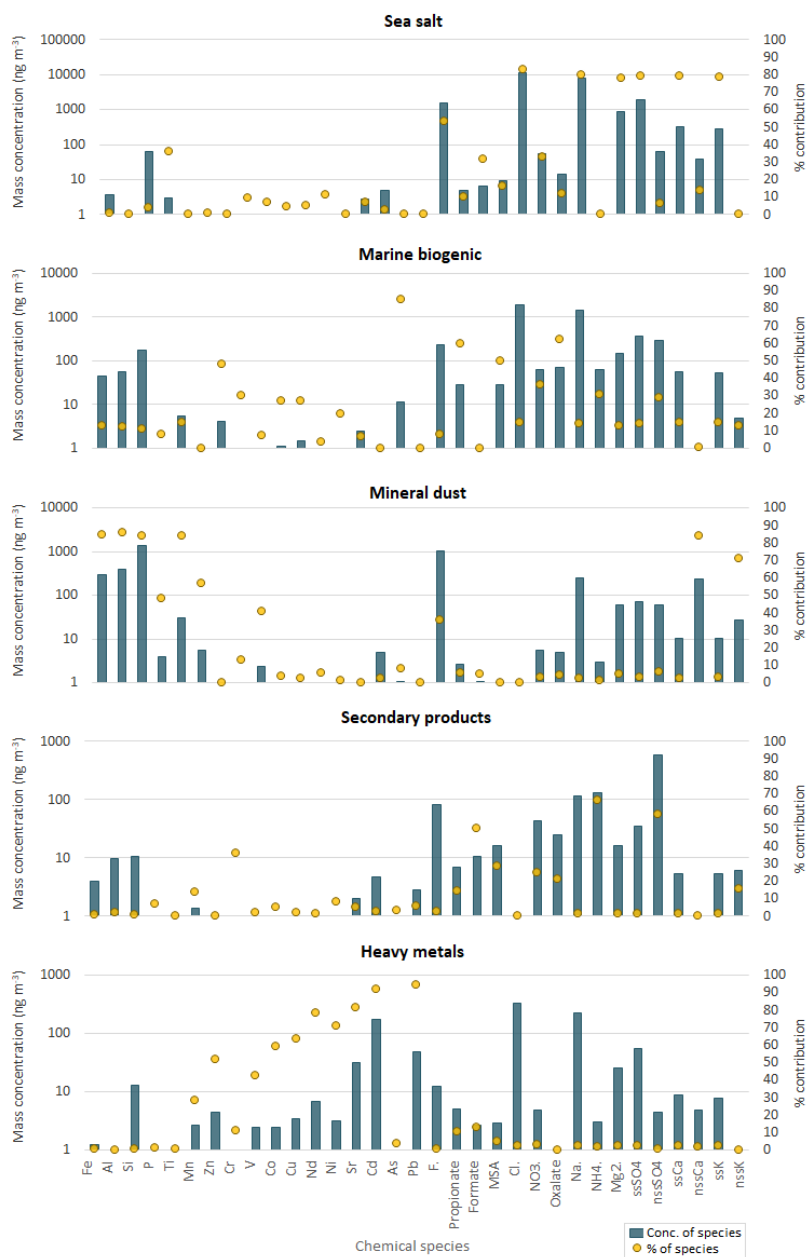


1050 **Figure 7.** Scatterplots for ratios of MSA (left) and NH_4^+ (right) to nss-SO_4^{2-} for 2016 (blue) and 2017 (orange).
 1051 Concentrations are expressed in $\mu\text{g m}^{-3}$. Note the logarithmic y-axis of the figure on the right.





1055 **Figure 8.** Profiles of the five sources identified by the PMF analysis. Blue bars denote the mass concentrations of individual
 1056 elements/ionic species (left logarithmic axis, ng m^{-3}) while the yellow points indicate the percent of species attributed to
 1057 the source (right axis).



1058